

SUB-PHOTOSPHERIC SHOCKS IN RELATIVISTIC EXPLOSIONS

ANDREI M. BELOBORODOV

Physics Department and Columbia Astrophysics Laboratory, Columbia University, 538 West 120th Street, New York, NY 10027, USA
Draft version January 18, 2017

ABSTRACT

This paper examines the mechanism of internal shocks in opaque relativistic outflows, in particular in cosmological gamma-ray bursts. The shocks produce neutrino emission and affect the observed photospheric radiation from the explosion. They develop from internal compressive waves and can be of different types depending on the composition of the outflow: (1) Shocks in “photon gas,” with negligible plasma inertia, have a unique structure determined by the force-free condition—zero radiation flux in the plasma rest frame. Radiation dominance over plasma inertia suppresses formation of collisionless shocks mediated by collective electromagnetic fields. (2) If the outflow is sufficiently magnetized, a strong collisionless subshock develops, which is embedded in a thicker radiation-mediated structure. (3) Waves in outflows with a free neutron component lead to dissipation through nuclear collisions. At large optical depths, shocks have a thickness comparable to the neutron free path, with an embedded radiation-mediated and collisionless subshocks. The paper also presents first-principle simulations of magnetized flows filled with photons, demonstrating formation of shocks and their structure. Simple estimates show that magnetized sub-photospheric shocks are efficient producers of photons and have a great impact on the observed photospheric radiation. The shock structure changes as the outflow expands toward its photosphere. The dissipation is accompanied by strong e^\pm pair creation, and the e^\pm -dressed shock carries the photosphere with it up to two decades in radius, emitting a strong pulse of nonthermal radiation.

Subject headings: magnetohydrodynamics (MHD) – neutrinos — radiation mechanisms: non-thermal – radiative transfer – shock waves — gamma-rays bursts: general

1. INTRODUCTION

Astrophysical explosions and jets generate shock waves, which produce radiation. Their radiative properties are determined by the dissipation mechanism that sustains the velocity jump in the shock and by its ability to generate nonthermal particles. This paper examines the mechanism of internal shocks in gamma-ray bursts (GRBs) that occur before the GRB jets become transparent to radiation. The approach and some of the results may also be of interest for other explosions, e.g. in novae or supernovae.

1.1. *Internal shocks in GRB jets*

The main features of GRB explosions may be summarized as follows: the outflow is relativistic, it carries magnetic fields frozen in fully ionized plasma, and a large fraction of its energy is carried by neutral particles — photons and free neutrons. GRB outflows start very opaque near the central engine of the explosion and become transparent at a large “photospheric” radius R_\star . Internal shocks can develop below and above the photosphere.

Early works proposing internal shocks in GRBs focused on shocks above the photosphere (Rees & Mészáros 1994; Kobayashi et al. 1997; Daigne & Mochkovitch 1998). They can only be collisionless, i.e. mediated by collective electromagnetic fields. Their mechanism has been studied in detail using particle-in-cell simulations, and it was found that the presence of transverse magnetic fields renders the shock unable to accelerate particles (Sironi & Spitkovsky 2011): the postshock electron-ion plasma is in a two-temperature state, $T_e < T_i$, with electrons and ions forming nearly Maxwellian distributions. This

may, however, change if the electron-ion outflow is loaded with e^\pm plasma. Ultra-relativistic shocks in e^\pm -loaded plasma with transverse magnetic field were found capable of accelerating positrons (Hoshino et al. 1992; Amato & Arons 2006; Stockem et al. 2012).

Shocks in opaque plasma below the photosphere R_\star are less explored and may be key to understanding GRB emission (Mészáros & Rees 2000b; Pe’er et al. 2006; Beloborodov 2010; Levinson 2012). There is significant evidence that GRB radiation is mainly produced below the photosphere (Ryde et al. 2011; Beloborodov 2013; Yu et al. 2015), and detailed simulations of radiative transfer in opaque heated jets give spectra consistent with GRB observations (Vurm & Beloborodov 2016). Internal shocks provide a plausible mechanism for sub-photospheric heating invoked by these models.

Internal shocks may result from the fast variability of the central engine or the outflow interaction with the progenitor star (e.g. Lazzati et al. 2013; Ito et al. 2015). At later stages of ballistic expansion with a high Lorentz factor Γ , internal shocks at radius r can develop from velocity variations on scale $L \sim r/\Gamma$ (measured in the outflow rest frame). This scale also sets the characteristic optical depth seen by photons in the expanding outflow, $\tau_T \sim \sigma_T n_e L$, where σ_T is Thomson cross section and n_e is the proper density of electrons and positrons.

The present paper is motivated by the following questions:

- (1) Can sub-photospheric shocks be collisionless? This is assumed in models of TeV neutrino emission from the jet-progenitor interaction (Razzaque et al. 2003), however the assumption is questionable (Murase & Ioka 2013).
- (2) Is the shock capable of producing high-energy par-

ticles? The presence of high-energy electrons at large optical depths would have a strong effect on the photospheric radiation (Pe’er & Waxman 2004; Beloborodov 2010; Vurm & Beloborodov 2016).

(3) How does the shock evolve as it emerges from the photosphere and what is its observational appearance?

1.2. Radiation-mediated shocks (RMS)

Since GRB jets carry a large number of photons per electron, sub-photospheric shocks are naturally expected to be mediated by radiation (Levinson 2012). Then dissipation and the profile of the velocity jump are controlled by photon scattering.

Basic features of radiation-mediated shocks (RMS) were studied in the 1950s (see Zeldovich & Raizer 1966 and refs. therein). The RMS propagation is sustained by radiation diffusion: radiation generated by the shock diffuses upstream and pre-heats the upstream gas. This creates a pressure gradient, a kind of a “pillow” that allows the gas to smoothly decelerate, avoiding the collapse of the shock thickness to the collisionless scale (the ion Larmor radius).

The first RMS models assumed that radiation is everywhere in local thermodynamic equilibrium. This assumption can be strongly violated in astrophysical explosions, as the timescale to establish thermodynamic equilibrium can be much longer than the time it takes the gas to cross the shock. Models relaxing the equilibrium assumption have been developed and applied to supernova shock breakout (e.g. Weaver 1976; Sapir et al. 2013). The RMS model was also extended to relativistic shocks (Levinson & Bromberg 2008; Budnik et al. 2010; Bromberg et al. 2011; Levinson 2012). The highest temperature achieved in the RMS depends on the photon number carried by the upstream through the shock. Levinson (2012) emphasized the low efficiency of photon production by the RMS in GRB jets and developed a shock model with a conserved photon number.

The RMS thickness is large, comparable to or larger than the photon mean free path. This inhibits diffusive acceleration of charged particles. In particular, electrons radiate energy faster than they can cross the shock. The RMS is only capable of a slow diffusive acceleration of photons up to the MeV band (in the shock frame).

The RMS picture of internal shocks has, however, a few caveats. Previous work did not take into account that the outflow is magnetized, and the magnetic field can change the RMS structure and the dissipation mechanism. In addition, GRB explosions are expected to carry free neutrons; their collisions can play a key role in shaping the shock waves at large optical depths and offer an additional mechanism for producing high-energy particles and neutrinos.

1.3. Outline of the paper

We begin with basics of shock formation. Section 2 examines how a super-sonic compressive wave steepens and launches a pair of shock waves. We first describe shock formation in a polytropic gas using the hydrodynamic approximation (zero mean free path of all particles and photons). Then we relax this approximation and discuss the role of photon diffusion in the formation of RMS and collisionless shocks. We consider a “cold” gas with sound

speed $c_0 \ll c$ and formulate two conditions for the immediate RMS formation (vs. formation of a collisionless shock). We also discuss flows with large c_0 , including the extreme regimes where the flow inertia is dominated by radiation ($c_0 = c/\sqrt{3}$) or magnetic fields ($c_0 = c$).

Section 3 describes the general jump conditions for shocks in media with any thermal pressure and magnetization. A moderate magnetization of the flow changes the jump conditions and we argue that this leads to the formation of a thin collisionless subshock, even at large optical depths. We evaluate the region in the parameter space where a strong collisionless subshock must exist.

Section 4 focuses on shocks in “photon-gas” with subdominant magnetic fields and negligible plasma inertia ($c_0 = c/\sqrt{3}$). This regime may occur in GRB explosions at their early stages, during the jet breakout and its acceleration by radiation pressure. We use a self-consistent simulation of time-dependent radiative transfer and obtain the solution for the shock structure.

Then Section 5 presents the RMS structure at later stages when the plasma inertia becomes important. As the main tool, we use direct Monte-Carlo simulations of time-dependent radiative transfer coupled with the flow dynamics. We first investigate RMS formation in a weakly magnetized flow, and discuss the effect of bulk Comptonization and e^\pm creation inside the shock front. Then we turn to shocks in a magnetized fluid and demonstrate the formation of a strong collisionless subshock embedded in the RMS, as anticipated in Section 3.

Section 6 investigates how plasma heating in a collisionless (sub)shock results in “breeding” of e^\pm pairs. Section 7 discusses the emergence of a e^\pm -dressed shock from the photosphere.

Section 8 describes shocks in outflows with a free neutron component. Due to their large free paths, neutrons introduce a large effective viscosity. Nuclear collisions produce ultra-relativistic e^\pm pairs and neutrinos. They sustain broad shock fronts until the jet reaches the neutron decoupling radius R_n where most neutrons begin to flow freely without collisions.

The results and their implications for GRB models are discussed in Section 9.

2. FORMATION OF SHOCKS

2.1. Ballistic approximation and caustics

Consider an outflow with internal supersonic motions. Such motions can be approximately described as ballistic: each fluid element is moving with a constant velocity. It is well known that ballistic flows create caustics — surfaces where density diverges (in cosmology such surfaces are called Zeldovich pancakes).

The flow near the caustic is approximately plane-parallel (one-dimensional). It is convenient to view the flow in the rest frame of the caustic and choose the x -axis normal to it, so that the flow converges toward $x = 0$ along the x -axis with velocity $v(t, x)$. Since $\beta = v/c$ may approach unity in relativistic flows, it is useful to introduce dimensionless momentum $p = \gamma\beta$ where $\gamma = (1 - \beta^2)^{-1/2}$. Velocity is related to p by

$$v = \frac{cp}{(1 + p^2)^{1/2}}. \quad (1)$$

A simple example of a converging flow is provided by

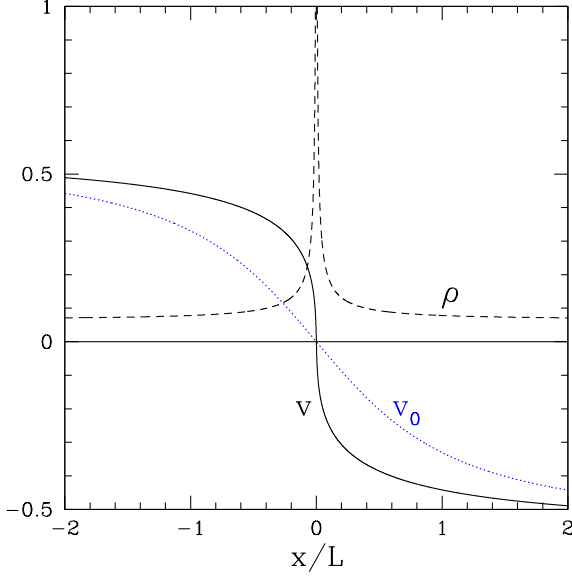


FIG. 1.— Fluid velocity $v(x)$ (in units of c) and density $\rho(x)$ (arbitrary units) evolving in the ballistic compressive wave with the initial profile $v_0(x_0)$ given by Equation (2), with $p_{\max} = 0.7$. The initial velocity profile is shown by the dotted curve, and the next snapshot is taken at the time of caustic formation $t_c \approx 2.24L/c$. The dashed curve shows density ρ at $t = t_c$; the initial density at $t = 0$ was uniform.

an initial arctan profile,

$$p_0(x) = -p_{\max} \frac{2}{\pi} \arctan \frac{x}{L}. \quad (2)$$

The ratio p_{\max}/L describes the initial steepness of the wave, and p_{\max} describes its amplitude. The wave is non-relativistic if $p_{\max} \ll 1$. The characteristic timescale of the profile evolution is $t_c = L/cp_{\max}$. On this timescale the ballistic wave steepens (Figure 1) and the caustic forms at $x = 0$, where $-\partial v/\partial x$ is maximum.

The density of the ballistic flow diverges at the caustic. Its evolution is determined by the relation

$$x(x_0, t) = x_0 + v_0 t, \quad (3)$$

where x_0 is the initial position of the fluid slab dx_0 at times $t_0 \ll t_c$, and $v_0(x_0) = v_0(x)$ is the initial velocity profile. The slab dx_0 is contracting by the factor $(\partial x/\partial x_0) = 1 + (dv_0/dx_0)t$. Therefore, the evolution of baryon density ρ is described by

$$\rho(x_0, t) = \frac{\rho_0(x_0)}{1 + v'_0 t}, \quad v'_0 = \frac{dv_0}{dx_0}, \quad (4)$$

where $\rho_0(x_0) = \rho_0(x)$ is the density at $t_0 \ll t_c$. The compression rate is highest at $x = 0$ and here density diverges at time

$$t_c = - \left(\frac{dv_0}{dx_0} \right)^{-1}_{x_0=0} = \frac{\pi L}{2cp_{\max}}. \quad (5)$$

At this moment, $v(x)$ becomes discontinuous at $x = 0$.

2.2. Pressure build-up in the converging flow

True caustics form in flows with zero pressure. A small initial pressure $P_0 \neq 0$ qualitatively changes the picture:

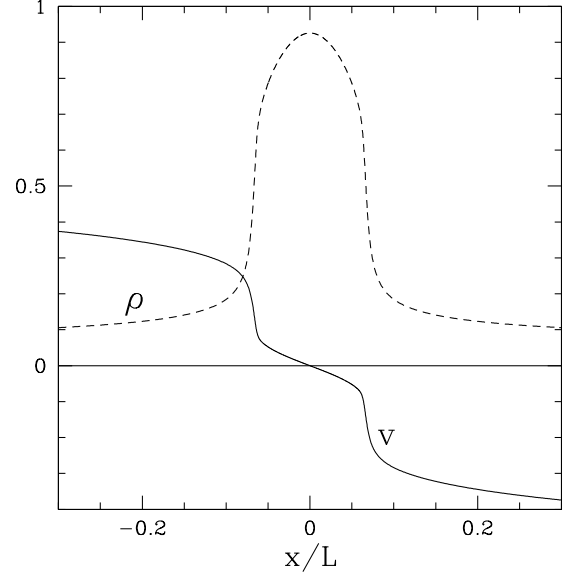


FIG. 2.— Snapshot of the evolved compressive wave with the same initial conditions as in Figure 1 but with a finite initial pressure. The flow has the initial sound speed $c_0 = 0.1c$ and adiabatic index $\alpha = 4/3$. The snapshot is taken at $t \approx 2.8L/c$, shortly before the formation of a pair of shocks.

it can be strongly amplified in the converging flow near $x = 0$ and the generated pressure gradient stops the flow.

The deceleration of the converging flow around $x = 0$ accelerates the steepening of the velocity profile on each side of the caustic (Figure 2). As a result, at some time t_* and locations $\pm x_*$ two shocks form and continue to propagate away from $x = 0$. The type of the nascent shock depends on the physical conditions in the region $x \sim x_*$. Below we discuss the pressure build up in the converging flow, then estimate the location of shock formation x_* and the corresponding maximum compression.

One source of pressure is the thermal motions of plasma particles. It grows in the converging flow, however its contribution to the total pressure is limited by fast radiative cooling, which converts plasma heat to radiation. In a local thermodynamic equilibrium, radiation strongly dominates the heat capacity of GRB jets, because the photon density n_γ greatly exceeds the plasma density. At small radii, where the e^\pm population is in annihilation equilibrium with Planck radiation, one finds $n_\pm/n_\gamma \approx (kT/m_e c^2)^{-3/2} \exp(-2m_e c^2/kT)$ (Svensson 1984); the e^\pm abundance is decreasing exponentially in the expanding and adiabatically cooling jet. At larger radii, the particle density (ions, e^- , or e^+) does not exceed $\sim 10^{-3}n_\gamma$ and, in a local thermodynamic equilibrium, this implies a plasma pressure $P_{\text{pl}} \ll P_{\text{rad}}$. Here we examine compressive waves in a medium that is initially not too far from thermal equilibrium¹ and thus has $P_{\text{pl}} \ll P_{\text{rad}}$. Then the two main sources of pressure that can be amplified in the wave are radiation and the transverse magnetic field.

¹ Shocks create strong deviations from thermodynamic equilibrium, and these deviations become long-lived in the region of moderate optical depth, around and above the photosphere. New shocks in this region will develop in the plasma with hot (thermally decoupled) ions, preheated by previous shocks.

Magnetic fields are expected to carry a significant fraction ϵ_B of the jet energy. Comparison of theoretical GRB spectra with observations suggests $\epsilon_B \sim 0.01 - 0.1$ (Vurm & Beloborodov 2016). The jet plasma is an excellent conductor, so the magnetic field is frozen in it and advected by the flow. In an internal compressive wave, the frozen transverse field is compressed together with the plasma: $B \propto \rho$ or $\mathcal{B} \propto \tilde{\rho}$, where $\mathcal{B} = B/\gamma$ is the magnetic field measured in the fluid frame, $\tilde{\rho} = \rho/\gamma$ is the proper density of the fluid, and γ is its Lorentz factor. The magnetic pressure grows in the converging flow as²

$$P_B = \frac{\mathcal{B}^2}{8\pi} \propto \tilde{\rho}^2. \quad (6)$$

The growth of radiation pressure P_{rad} depends on its ability to diffuse out of the compressed region, which depends on the optical depth. If the flow is sufficiently opaque to photons, the radiation will be trapped and

$$P_{\text{rad}} = \frac{U_{\text{rad}}}{3} \propto \tilde{\rho}^{4/3} \quad (\text{trapped radiation}). \quad (7)$$

In the opposite limit, when the compressed region is transparent to photons, there is no significant amplification of P_{rad} .

Equations (6) and (7) both have a polytropic form $P \propto \tilde{\rho}^\alpha$, with $\alpha = 2$ or $4/3$. A similar relation could also be used for compressive waves in a medium that is far from thermal equilibrium with radiation and filled with hot, thermally decoupled, ions (protons). The proton pressure in the compressive wave follows the relation $P_p \propto \tilde{\rho}^\alpha$ with $\alpha \approx 5/3$ as long as the proton temperature is non-relativistic, $kT_p \lesssim m_p c^2$.

2.3. Shock formation in non-relativistic polytropic gas

Let us first consider a non-relativistic gas, $P \ll \tilde{\rho} c^2$. Suppose that initially the gas has uniform pressure P_0 and density $\tilde{\rho}_0$, and is set in motion with velocity $v_0(x)$ that corresponds to momentum profile $p_0(x)$ given e.g. by Equation (2). We assume that the peak of velocity profile $v_{\text{max}} = cp_{\text{max}}(1 + p_{\text{max}}^2)^{-1/2}$ is much greater than the sound speed $c_0 = (\alpha P_0/\tilde{\rho}_0)^{1/2}$. In the ballistic approximation, the profile would develop a caustic at $x = 0$ at time t_c . We wish to know how the finite pressure changes the flow dynamics, in particular what is the maximum pressure achieved in the compressed region before a shock forms, and where the shock formation occurs.

Even if the compressive wave is relativistic, $p_{\text{max}} \gtrsim 1$, the condition $c_0 \ll c$ implies that the shocks form not far from $x = 0$ where $v_0(x)$ is non-relativistic. Therefore, the shock formation can be examined using Newtonian hydrodynamics around $x = 0$, so we will use $\gamma \approx 1$, $\tilde{\rho} \approx \rho$, and $\mathcal{B} \approx B$.

The evolution of the gas is convenient to view on the x - t plane (Figure 3). Each streamline is described by $x(x_0, t)$ where x_0 is the Lagrangian coordinate — the position at $t = 0$. Initially, a small fraction of gas is in the subsonic region $|v_0| < c_0$ near $x = 0$. The streamlines that start outside this region are initially supersonic and eventually become subsonic.

² P_B and $\tilde{\rho}$ are measured in the same (fluid) frame. Pressure and internal energy density are always measured in the fluid frame and we omit tilde to simplify notation.

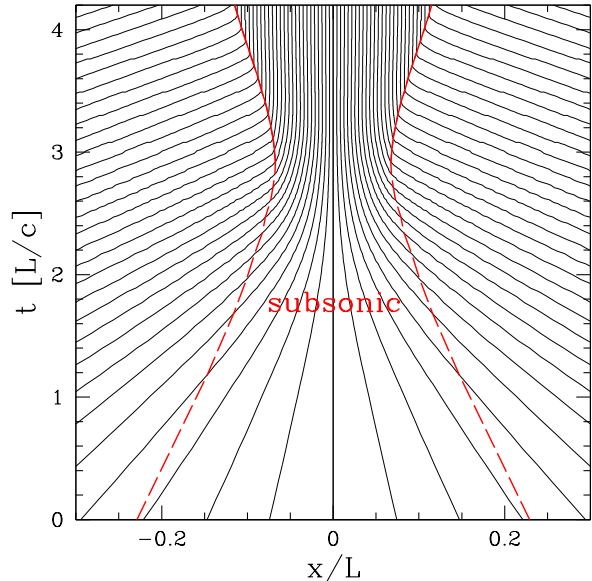


FIG. 3.— The streamlines on the spacetime diagram. The gas has the initial velocity profile $v_0(x_0)$ given by Equation (2) with $p_{\text{max}} = 0.7$, the initial sound speed $c_0 = 0.1c$, and the adiabatic index $\alpha = 4/3$. The boundary of the subsonic region $v < c_s$ is shown by the red curves. The red curve is dashed where the deceleration to the subsonic speed occurs smoothly and solid where the deceleration occurs through a shock. The shock forms at $t_* \approx 2.9L/c$ and $x_* \approx 0.07L$.

There is a critical Lagrangian coordinate x_0^* . Streamlines that start at $|x_0| < x_0^*$ will become subsonic without a shock: the compressed gas is gradually decelerated as its specific kinetic energy $v_0^2/2$ gets transformed into enthalpy $(U + P)/\rho = c_s^2/(\alpha - 1)$, where $c_s^2 = c_0^2(\rho/\rho_0)^{\alpha-1}$ is the local speed of sound. This “compressive deceleration” to a subsonic speed occurs when the compression factor ρ/ρ_0 satisfies

$$\frac{c_0^2}{\alpha - 1} \left(\frac{\rho}{\rho_0} \right)^{\alpha-1} \approx \frac{v_0^2}{2}. \quad (8)$$

Approximating the streamline before this moment as ballistic, one can estimate $\rho_0/\rho = 1 + v_0'(x_0)t$. Therefore, the deceleration time $t_{\text{dec}}(x_0)$ at which the streamline with Lagrangian coordinate x_0 becomes subsonic may be estimated from the condition,

$$(1 + v_0' t_{\text{dec}})^{\alpha-1} \approx \frac{2c_0^2}{(\alpha - 1)v_0^2}. \quad (9)$$

The corresponding location on the streamline is

$$x_{\text{dec}} \approx x_0 + v_0 t_{\text{dec}}. \quad (10)$$

The smooth compressive deceleration is only possible for streamlines with sufficiently small $|x_0| < x_0^*$. For large $|x_0|$ one finds $t_{\text{dec}} > |x_0/v_0|$, and the compressive deceleration becomes impossible — the ballistic flow does not have a chance to compress enough before it hits the existing subsonic region near $x = 0$. Then the deceleration occurs through a shock.

The critical Lagrangian coordinate x_0^* at which the

shock forms is given by (see Appendix A),

$$\frac{x_0^*}{L} \approx 3 \left(\frac{c_0}{cp_{\max}} \right)^{1/\alpha}. \quad (11)$$

The compression of gas with the Lagrangian coordinate x_0^* is determined by Equation (8) with v_0 evaluated at x_0^* . In the limit of $x_0^* \ll L$, the compression along this streamline is given by

$$\frac{\rho_\star}{\rho_0} = \frac{x_0^*}{x_\star} \sim \left(\frac{cp_{\max}}{c_0} \right)^{2/\alpha}. \quad (12)$$

It determines the maximum pressure developed in the flow before the shock is launched,

$$P_\star = P_0 \left(\frac{\rho_\star}{\rho_0} \right)^\alpha \sim P_0 \left(\frac{cp_{\max}}{c_0} \right)^2 \sim p_{\max}^2 \rho_0 c^2. \quad (13)$$

The maximum pressure is comparable to the peak kinetic energy density of the wave, even though P_\star only develops in a small region near the caustic $x \approx 0$ where the flow momentum is much smaller than p_{\max} . This is because P_\star is controlled by the *curvature* of the velocity profile (described by $v_0'''(0)$, see Appendix A), which depends on p_{\max} .

At t_\star and x_\star the sound speed of the ballistic flow is not much below its bulk speed $v \sim v_0(x_0^*)$, so the nascent shock is not strong. Then the shock propagates through the ballistic gas with increasing Lagrangian coordinate $|x_0|$ where the upstream velocity $v_0(x_0)$ is higher, and the shock compression ratio quickly approaches the strong-shock limit $(\alpha + 1)/(\alpha - 1)$.

2.4. Shock formation in relativistic polytropic gas

Shock formation in relativistic gas $P \gg \tilde{\rho}c^2$ may be examined in a similar way. This regime occurs in relativistic explosions at small radii where radiation dominates the gas inertia. Then $c_0^2 = c^2/3$ (Landau & Lifshitz 1959), and one must consider relativistic compressive waves with $v_{\max} > c_0$.

The flow is initially subsonic in the zone where $|p_0| < 2^{-1/2}$. Outside this zone the flow is approximately ballistic and its density is growing with time as $(1 + v_0' t)^{-1}$, where $v_0' = c(dp_0/dx_0)\gamma_0^{-3}$. The compressive deceleration of the relativistic gas is quite efficient: a large fraction of the bulk kinetic energy is converted to enthalpy when the gas is compressed by only a factor of ~ 2 .

However, even such a moderate compression is difficult to achieve in the relativistic ballistic flow, because the gas with $\gamma_0 \gg 1$ ($v_0 \approx c$) has a small v_0' and hence it is compressed slowly. The maximum time allowed for ballistic compression is x_0/c and the corresponding maximum compression factor is

$$(1 + v_0'|x_0|/c)^{-1} \approx 1 \quad \text{if} \quad |p_0| \gg 1. \quad (14)$$

Gas with a relativistic p_0 ballistically hits the subsonic region before it has a chance for compressive deceleration. Thus, the shock must form at Lagrangian coordinate x_0^* such that $|p_0(x_0^*)| \sim 1$, not far from the boundary of the initial subsonic zone $|p_0| = 2^{-1/2}$. The time and location of shock formation are $t_\star \sim x_0^*/c$ and $x_\star \sim x_0^*/2$. The

shock forms with a mildly relativistic amplitude; it becomes ultra-relativistic when it propagates into the gas converging with $|p_0| \gg 1$.

One can also consider shock formation in a magnetically dominated gas $P_B \gg \tilde{\rho}c^2$ and $P_B \gg P_{\text{rad}}$. Then $c_0 \approx c$ and it is convenient to define $\gamma_{c0} = (1 - c_0^2/c^2)^{-1/2}$. Shocks form in compressive waves with $v_{\max} > c_0$, which corresponds to Lorentz factor $\gamma_{\max} > \gamma_{c0}$.

In the limit of strong magnetization, the sound speed becomes equal to c and shocks do not form. In this case, the dynamic equations read $\partial_\mu T^{\mu\nu} = 0$ with the stress-energy tensor components

$$T^{tt} = \frac{B^2 + E^2}{8\pi}, \quad T^{tx} = \frac{EB}{4\pi}, \quad T^{xx} = \frac{B^2 + E^2}{8\pi}, \quad (15)$$

(the magnetic field \mathbf{B} is assumed to lie in the y - z plane perpendicular to the fluid velocity). The neglect of the plasma contribution to $T^{\mu\nu}$ defines so-called force-free electrodynamics, where plasma only serves to conduct electric currents demanded by $\nabla \times \mathbf{B}$ and supplies no inertia. The plasma velocity $v = \beta c$ is related to the electric field by $\mathbf{E} + \mathbf{v} \times \mathbf{B}/c = 0$ and $\beta = E/B$. Adding and subtracting the energy and momentum conservation laws,

$$\frac{\partial T^{tt}}{\partial t} + c \frac{\partial T^{tx}}{\partial x} = 0, \quad \frac{\partial T^{tx}}{\partial t} + c \frac{\partial T^{xx}}{\partial x} = 0, \quad (16)$$

one obtains

$$\frac{\partial u_\pm}{\partial t} \pm c \frac{\partial u_\pm}{\partial x} = 0, \quad u_\pm = (1 \pm \beta) B. \quad (17)$$

The initial profiles of $u_\pm(0, x) = f_\pm(x)$ determine $u_\pm(t, x) = f_\pm(x \mp ct)$. This gives explicit solutions for $B = (u_+ + u_-)/2$ and $\beta = (u_+ - u_-)/(u_+ + u_-)$, demonstrating their smooth behaviour, with no caustics or shocks.

2.5. Radiation diffusion and formation of RMS

Radiation diffusion is an essential ingredient of an RMS, since it is the mechanism of shock propagation. However, too fast diffusion would let radiation escape, inhibiting the RMS formation. A shock wave is usually assumed to be radiation-mediated if two conditions are satisfied:

(A) The jump conditions give in the downstream $P \approx P_{\text{rad}}$, so that a large fraction of energy generated by the shock is carried by radiation (Zeldovich & Raizer 1966).

(B) The medium has optical depth $\tau > c/v_0$, so that the shock generates radiation faster than it could diffuse out of the system of size L . For instance, in a supernova explosion one could take L as the radius of the expanding ejecta (e.g. Tolstov et al. 2013).

In fact, these conditions do not guarantee that the shock is mediated by radiation. The velocity profile connecting the upstream and downstream may contain a “subshock” — a sharp jump mediated by the plasma on a scale much smaller than the photon free path to scattering. In non-relativistic shocks ($v_0 \ll c$) satisfying conditions (A) and (B) the velocity profile is smooth, with no subshock (Zeldovich & Raizer 1966). However, in the relativistic case,

$v_0 \approx c$, a weak subshock was reported (Budnik et al. 2010). In addition, in the above condition (B) one should be careful with what is meant by the “size of the system.”

Consider a compressive wave of a mildly relativistic amplitude $v_{\max} \sim c$ and length $\sim L$. A characteristic optical depth may be defined as

$$\tau_L = L\rho_0\kappa, \quad (18)$$

where κ is the opacity of the gas. Suppose the unperturbed gas has a non-relativistic sound speed $c_0 \ll c$. Section 2.3 described how at time $t_\star \sim L/c$ two shocks form near the caustic, at the Lagrangian coordinate $x_0^*/L \sim (c_0/c)^{1/\alpha}$. Thus, the region of shock formation has the optical depth

$$\tau_\star \sim \tau_L \left(\frac{c_0}{c} \right)^{1/\alpha}. \quad (19)$$

For a radiation-dominated flow, $P \approx P_{\text{rad}}$ and $\alpha = 4/3$. In this case, however, Equation (19) can only be used if radiation is trapped, i.e. unable to diffuse out of the region of shock formation on the timescale x_\star/v_0^* . This requires

$$\tau_\star \gg \frac{c}{v_0^*}, \quad (20)$$

where $v_0^* \approx c\tau_\star/\tau_L$ is the flow velocity upstream of the nascent shock. The trapping condition is satisfied if

$$\frac{c_0}{c} \gg \tau_L^{-2/3}. \quad (21)$$

For the flow with the upstream pressure P_0 dominated by radiation, one can use the relation

$$\frac{c_s}{c} \approx \left(\frac{w}{3} \right)^{1/2}, \quad w \equiv \frac{U_{\text{rad}} + P_{\text{rad}}}{\tilde{\rho}c^2}. \quad (22)$$

Then condition (21) may also be written as $w \gg 3\tau_L^{-4/3}$. If this condition is satisfied, a propagating jump in radiation pressure will develop at t_\star , and the nascent shock will be mediated by photons, i.e. an RMS will be launched.

The RMS velocity profile is shaped by the competition between advection of radiation through the shock and its diffusion in the opposite, upstream direction. Therefore, the optical depth of the velocity jump $\Delta\tau$ is regulated to

$$\Delta\tau \sim \frac{c}{v_0}. \quad (23)$$

The RMS propagation involves continual amplification of radiation advected through the shock — the result of photon scattering in the region of a steep velocity gradient. As the hot downstream photons diffuse back into the upstream, they experience “bulk Comptonization” — they are boosted in energy by the factor of $\sim \gamma_0^2 = (1 - v_0^2/c^2)^{-1}$. As a result, the energy of radiation advected through the shock is amplified, as required by the jump conditions for a propagating shock.

Launching an RMS at t_\star requires an initial build-up of radiation density $\sim \rho v_0^{*2}/2$ near the shock front, which is only possible if the trapping condition (21) is satisfied. Otherwise, radiation leaks out of the compressed region to large distances x . This may be viewed as a violation of RMS condition (B), as the effective “size of the system” during the shock formation is comparable to $x_\star \ll L$.

Then the radiation pressure gradient is too weak to control the velocity profile of the flow. Radiation is unable to resist the steepening of the velocity profile, and the width of the velocity jump is quickly reduced to the ion Larmor radius, forming a collisionless shock mediated by the collective electromagnetic field. It may later evolve into an RMS, when the postshock region has accumulated a sufficient optical depth, if there is enough time for that in the expanding outflow, i.e. if the shock forms sufficiently deep below the photosphere.

2.6. Critical magnetization

When both magnetic field and radiation contribute to pressure, there are two contributions to the sound speed, $c_s^2 = c_{\text{rad}}^2 + c_B^2$. It is convenient to define the dimensionless enthalpy of the flow,

$$w = \frac{P_{\text{rad}} + U_{\text{rad}}}{\tilde{\rho}c^2} = \frac{4P_{\text{rad}}}{\tilde{\rho}c^2}. \quad (24)$$

A similar quantity for the magnetic field \mathcal{B} in the fluid frame is

$$\sigma = \frac{P_B + U_B}{\tilde{\rho}c^2} = \frac{\mathcal{B}^2}{4\pi\tilde{\rho}c^2}. \quad (25)$$

Suppose the optical depth is large so that the radiation trapping condition is satisfied. The type of the nascent shock is determined by whether the magnetic field or radiation dominates the pressure in the compressed region near the caustic, $P_\star = P_{\text{rad}}^\star + P_B^\star$. An RMS forms if P_\star is dominated by radiation; otherwise, a collisionless shock is launched. Since P_\star must be the same in either case (see Equation 13), it is sufficient to compare the compressions needed to reach P_\star with only magnetic or only radiation pressure: $(P_\star/P_{\text{rad}})^{3/4}$ and $(P_\star/P_B)^{1/2}$. This comparison gives an approximate condition for launching a collisionless shock in a cold ($w_0 \ll 1$) and opaque medium,

$$\sigma_0 > \frac{w_0^{3/2}}{4p_{\max}}. \quad (26)$$

Note that this condition only applies to the nascent shock, at the point of maximum ballistic compression in the converging wave near the caustic. As the shock becomes stronger and continues to propagate into the ballistic flow where the upstream is less compressed (and hence less magnetized), its type may change.

An established steady shock structure is determined by the parameters of its upstream. The first step in the analysis of a steady propagating shock is the solution for its jump conditions.

3. SHOCK JUMP CONDITIONS

Jump conditions for relativistic magnetized shocks were studied by de Hoffmann & Teller (1950). Pulsar wind nebulae and GRBs revived interest to relativistic shocks. The upstream medium is usually assumed to be cold in the sense that its enthalpy is much smaller than the rest-mass energy of the plasma. This condition is not, however, satisfied in the inner regions of GRB jets. Below we write down the general jump conditions for shocks propagating in a hot magnetized plasma filled with radiation, and show their solutions.

Consider a shock wave propagating in a sufficiently extended, optically thick medium. Far upstream and far downstream of the shock the plasma and radiation can be described as an ideal gas with isotropic pressure. The thermal energy density U and pressure are related by

$$U = \frac{P}{\alpha - 1}, \quad (27)$$

where $\alpha = 4/3$, as long as U is dominated by radiation. When formulating the jump conditions we will keep α general, and specialize to $\alpha = 4/3$ in numerical solutions.

In the rest frame of the upstream (pre-shock) fluid, an observer will see the downstream (post-shock) fluid approaching with velocity \mathbf{v}_0 . The shock front is perpendicular to \mathbf{v}_0 and approaching with a higher velocity \mathbf{v}_1 parallel to \mathbf{v}_0 . The plasma carries a frozen magnetic field \mathcal{B} (measured in the fluid rest frame). We only consider magnetic fields perpendicular to the fluid velocity; a parallel magnetic field is anyway unchanged by the shock and hence does not affect the jump conditions.

3.1. Stress-energy tensor and sound speed

The stress-energy tensor of a hot magnetized flow with four-velocity $u^\mu = (\gamma c, \gamma \mathbf{v})$ is given by

$$T^{\mu\nu} = (\tilde{\rho}c^2 + U + P) \frac{u^\mu u^\nu}{c^2} + g^{\mu\nu} P + \frac{1}{4\pi} \left(F^{\sigma\mu} F^\nu_\sigma - \frac{g^{\mu\nu}}{4} F^{\sigma\delta} F_{\sigma\delta} \right), \quad (28)$$

where $\tilde{\rho}$ is the proper rest-mass density of the baryons, $g_{\mu\nu}$ is the metric tensor of Minkowski spacetime, and $F^{\mu\nu}$ is the electromagnetic tensor. Its electric and magnetic components in the lab frame, \mathbf{E} and \mathbf{B} , are related by $\mathbf{E} + \mathbf{v} \times \mathbf{B}/c = 0$, as the plasma is a nearly ideal conductor. Using $\mathbf{v} \perp \mathbf{B}$ and $B = \gamma \mathcal{B}$, the stress-energy tensor may be reduced to the ideal fluid form,

$$T^{\mu\nu} = H_{\text{eff}} \frac{u^\mu u^\nu}{c^2} + g^{\mu\nu} P_{\text{eff}}, \quad (29)$$

with the effective relativistic enthalpy and pressure

$$H_{\text{eff}} = \tilde{\rho}c^2 + U + P + \frac{\mathcal{B}^2}{4\pi}, \quad P_{\text{eff}} = P + \frac{\mathcal{B}^2}{8\pi}. \quad (30)$$

Before considering shocks, it is useful to examine sound waves in a uniform background that has $u^\mu_0 = (c, 0, 0, 0)$, $H_{\text{eff}}^0 = \text{const}$, and $P_{\text{eff}}^0 = \text{const}$. Let us consider longitudinal (compressive) waves propagating along the x -axis. In the linear order, perturbations are described by the four-velocity $u^\mu = (c, v, 0, 0)$, four-acceleration $u^\mu \nabla_\mu u^\nu = (0, \partial_t v, 0, 0)$, and compression $\nabla_\mu u^\mu = \partial_x v$. The linearized equations of motions $\nabla_\mu T^{\mu\nu} = 0$ give (for $\nu = t$ and $\nu = x$)

$$\frac{\partial H_{\text{eff}}}{\partial t} + H_{\text{eff}}^0 \frac{\partial v}{\partial x} - \frac{\partial P_{\text{eff}}}{\partial t} = 0, \quad (31)$$

$$H_{\text{eff}}^0 \frac{\partial v}{\partial t} + c^2 \frac{\partial P_{\text{eff}}}{\partial x} = 0. \quad (32)$$

These two equations can be reduced to the wave equation for v ,

$$\frac{\partial^2 v}{\partial t^2} - c_s^2 \frac{\partial^2 v}{\partial x^2} = 0, \quad (33)$$

where the wave speed c_s is defined by

$$c_s^2 dP_{\text{eff}} = c_s^2 d(H_{\text{eff}} - P_{\text{eff}}). \quad (34)$$

As the two main parameters of the fluid, it is convenient to use the dimensionless contributions of enthalpy and magnetic fields to the fluid inertia,

$$w \equiv \frac{U + P}{\tilde{\rho}c^2}, \quad \sigma \equiv \frac{\mathcal{B}^2}{4\pi\tilde{\rho}c^2}. \quad (35)$$

Then the wave speed defined in Equation (34) may be expressed as

$$\frac{c_s^2}{c^2} = \frac{(\alpha - 1)w + \sigma}{1 + w + \sigma}. \quad (36)$$

This general expression reduces to familiar cases in four limits:

- (1) $\sigma \ll w \ll 1$: $c_s^2 = \alpha P/\rho$ (non-relativistic sound waves),
- (2) $w \ll \sigma \ll 1$: $c_s^2 = B^2/4\pi\rho$ (non-relativistic fast MHD modes in a cold plasma),
- (3) $w \gg \sigma, 1$: $c_s^2 = (\alpha - 1)c^2 = c^2/3$ (sound waves in a relativistic gas), and
- (4) $\sigma \gg w, 1$: $c_s = c$ (force-free limit of the MHD modes).

Internal supersonic motions $v_0 > c_s$ generate shocks, as discussed in detail in Section 2. In addition, shocks can form through nonlinear steepening of sound waves excited by a subsonic perturbation, $v_0 < c_s$ (Zeldovich & Raizer 1966). The steepening occurs because c_s is slightly increased in the region compressed by the wave, so the crest of the wave (maximum $v > 0$ and maximum ρ) travels faster than the trough (minimum $v < 0$ and minimum ρ). Using Equation (36) one can verify that $dc_s/d\tilde{\rho} > 0$, i.e. compression indeed increases the local sound speed. The shock formed through sound-wave steepening propagates super-sonically but has a subsonic velocity jump, i.e. it separates regions with a relative velocity $v_0 < c_s$. Such weak shocks are found among the solutions shown below, along with strong shocks formed by supersonic motions $v_0 > c_s$.

Formation of shocks through steepening of sound waves is inefficient in the relativistic regimes (3) and (4), as in this case $dc_s/d\tilde{\rho} \rightarrow 0$ ($c_s = c/\sqrt{3}$ or $c_s = c$ is constant in both cases). In the force-free limit ($w \ll \sigma \gg 1$), shock formation does not occur at all (Section 2.4). In a radiation-dominated medium ($\sigma \ll w \gg 1$), shocks can be launched by a supersonic motion $v_0 > c/\sqrt{3}$.

3.2. Jump conditions

Jump conditions express the continuity of fluxes of energy, momentum, and baryon number in the rest frame of the shock front. The fluxes of energy and momentum are given by the stress-energy tensor $T^{\mu\nu}$ in Equation (29). The baryon flux is described by the four-vector

$$F^\mu = \tilde{\rho}u^\mu. \quad (37)$$

The fluxes along the shock normal (the x -axis) are given by

$$T^{tx} = \gamma p \tilde{\rho}c^2 (1 + w + \sigma), \quad (38)$$

$$T^{xx} = p^2 \tilde{\rho}c^2 (1 + w + \sigma) + P + \frac{\mathcal{B}^2}{8\pi}, \quad (39)$$

$$F^x = p \tilde{\rho}c, \quad (40)$$

where $p = \gamma\beta$, and P can be expressed in terms of w : $P = (1 - \alpha^{-1})w\hat{\rho}c^2$. Equating the fluxes upstream (index “u”) and downstream (index “d”) one obtains the relations,

$$\frac{T^{tx}}{cF^x} = \gamma_d (1 + w_d + \sigma_d) = \gamma_u (1 + w_u + \sigma_u), \quad (41)$$

$$\begin{aligned} \frac{T^{xx}}{cF^x} &= p_d (1 + w_d + \sigma_d) + \left(1 - \frac{1}{\alpha}\right) \frac{w_d}{p_d} + \frac{\sigma_d}{2p_d} \\ &= p_u (1 + w_u + \sigma_u) + \left(1 - \frac{1}{\alpha}\right) \frac{w_u}{p_u} + \frac{\sigma_u}{2p_u}. \end{aligned} \quad (42)$$

Given the upstream parameters p_u , w_u , σ_u , and taking into account that $p_d\sigma_d = p_u\sigma_u$ (implied by the flux freezing condition $\mathcal{B} \propto \hat{\rho}$), one can solve Equations (41) and (42) for the two unknowns p_d and w_d .

Typically, the upstream velocity relative to the downstream, v_0 , is a given in the shock problem. Therefore, we chose $p_0 = \gamma_0 v_0/c$ as an independent parameter instead of p_u . The upstream momentum in the shock frame, p_u , is related to the upstream momentum measured in the downstream frame, p_0 , by the Lorentz transformation between the two frames,

$$p_u = \gamma_d(p_0 + \beta_d\gamma_0). \quad (43)$$

For a given p_0 , a trial p_d determines $p_u(p_d)$, and the solution of Equations (41) and (42) (which is obtained numerically) yields p_d and p_u together with w_d .

The solutions are shown for $p_0 = 1$ and 10 in Figures 4 and 5, assuming $\alpha = 4/3$ (pressure is dominated by radiation). Figure 4 shows the compression ratio $\xi = \hat{\rho}_d/\hat{\rho}_u$ (which also determines $\sigma_d = \xi\sigma_u$) and Figure 5 shows the ratio w_d/σ_d . The latter determines the dissipation efficiency of the shock: if $w_d/\sigma_d > 1$ then a large fraction of the upstream energy goes to heat rather than ends up stored in the compressed magnetic field. The ratio w_d/σ_d is also interesting for another reason: it is related to the dissipation mechanism in the shock front, as discussed below.

3.3. Collisionless shocks

The jump conditions do not describe the structure or dissipation mechanism of the shock front. However, they allow one to evaluate the region in the parameter space where dissipation must be mainly collisionless.

We expect the shock to be mainly mediated by collective electromagnetic fields when the downstream enthalpy w_d is dominated by the compressed magnetic field σ_d . Then radiation cannot control the shock structure, as its pressure is below the ram pressure of the shock. In particular, in the limit of $w_d \ll \sigma_d$ the downstream can be approximated as a cold magnetized medium with negligible heat, so radiation has no effect on the upstream deceleration and the shock velocity profile; the profile inevitably steepens so that the entire velocity jump occurs in a thin layer on the collisionless plasma scale (gyroradius).

In contrast, in shocks with significant ratio w_d/σ_d , the diffusion of the postshock radiation into the upstream region creates a precursor that changes the upstream velocity and reduces the amplitude of the collisionless jump. The resulting structure may be described as a collisionless shock with a radiation precursor or, equivalently, an RMS with a collisionless subshock. In the limit

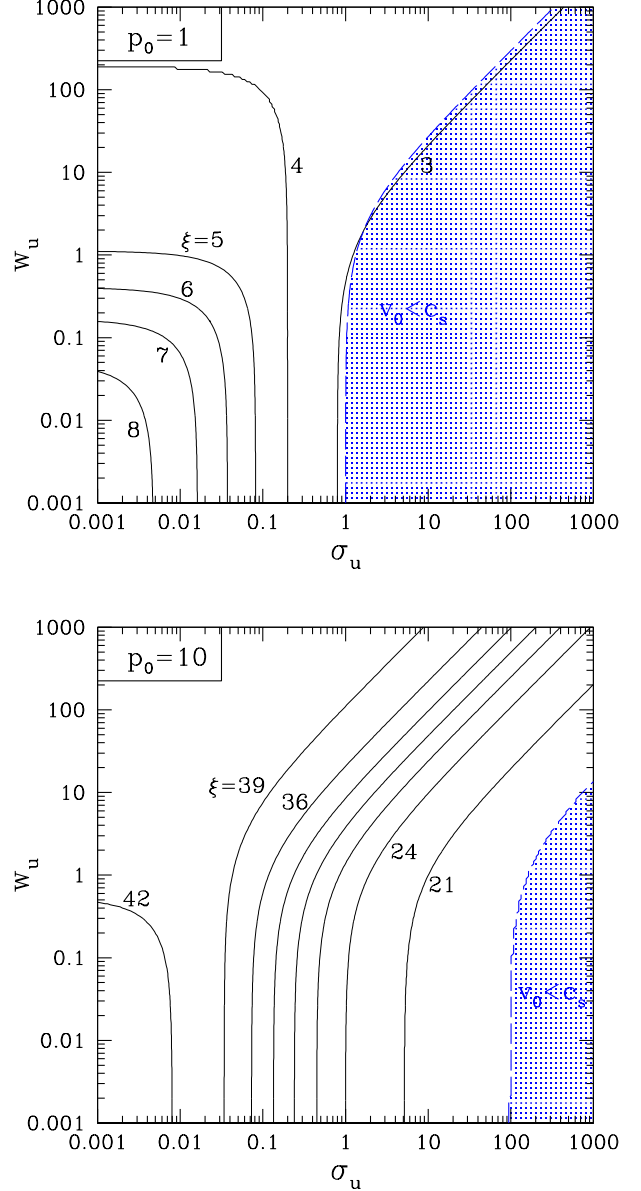


FIG. 4.— Compression ratio $\xi = \hat{\rho}_d/\hat{\rho}_u$ in a relativistic shock with $p_0 = 1$ (upper panel) and $p_0 = 10$ (lower level). The compression ξ depends on the upstream enthalpy w_u and magnetization σ_u . Solid curves show contours of the function $\xi(\sigma_u, w_u)$. The region where the shock is weak, $v_0 < c_s$, is dotted in blue and bounded by the dashed curve.

of $w_d \gg \sigma_d$, the subshock becomes weak or non-existent. Section 4 below demonstrates this fact for shocks in relativistic gas, $w \gg 1$, and Section 5 will show the shock structure for a moderate $w = 0.1$ with and without a significant magnetic field.

The transition between the two dissipation regimes — mainly mediated by collective electromagnetic fields and mainly mediated by radiation — occurs at $w_d/\sigma_d \sim 2$ (the shock structure in this transition region will be calculated in Section 5). The region where a strong collisionless jump is expected ($w_d/\sigma_d \lesssim 2$) is highlighted in red in Figure 5. We also show (in blue) the region where the shock is weak ($v_0 < c_s$) and could only form

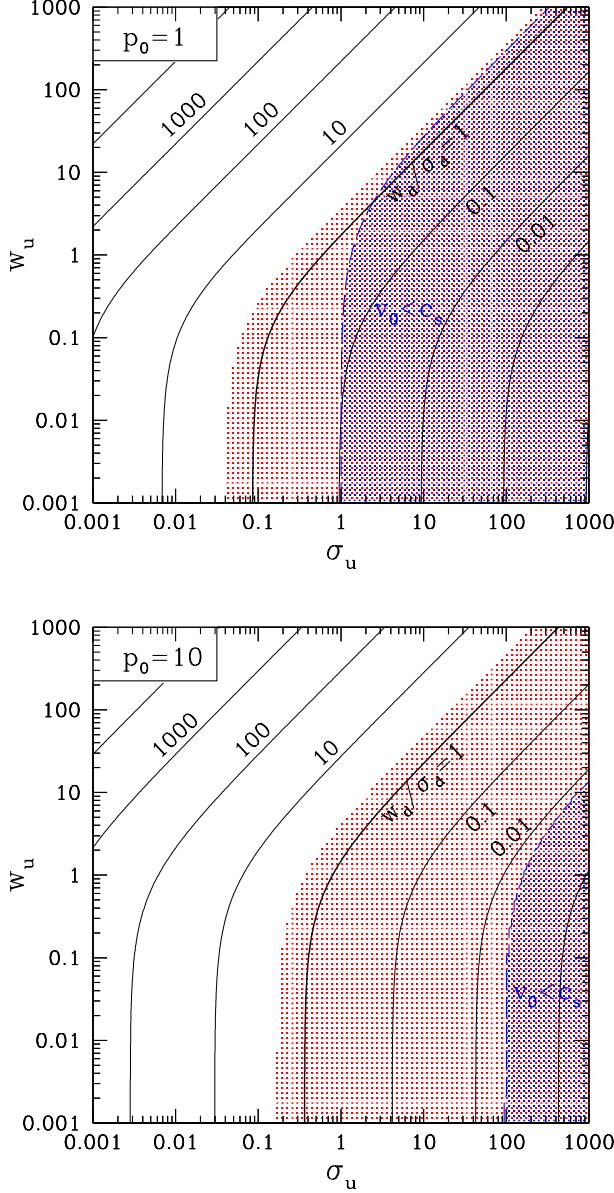


FIG. 5.— Ratio of the enthalpy and magnetization in the downstream, w_d/σ_d , for shocks with $p_0 = 1$ (upper panel) and $p_0 = 10$ (lower panel). This ratio depends on the upstream enthalpy w_u and magnetization σ_u ; the dependence is shown using contours on the σ_u - w_u plane. The blue region is the same as in Figure 4. Red dots highlight the region where $w_d < 2\sigma_d$. In this region, the shock is expected to have a strong collisionless jump where the velocity changes on a scale comparable to the gyroradius of the plasma particles.

through steepening of sound waves. As discussed in Section 3.1, such shocks do not easily form in a relativistic fluid ($w > 1$ or $\sigma > 1$) since steepening takes a long time, typically longer than the expansion time of the outflow. The region between the two curves $w_d = 2\sigma_d$ and $v_0 = c_s$ is where strong collisionless shocks occur. When $w_d \ll \sigma_d$ only a small fraction of the upstream kinetic energy is dissipated in the shock, and most of it ends up stored in the compressed magnetic field. Therefore, the strongest collisionless dissipation is expected if $w_d \sim \sigma_d$.

For a medium with a given enthalpy w_u one can de-

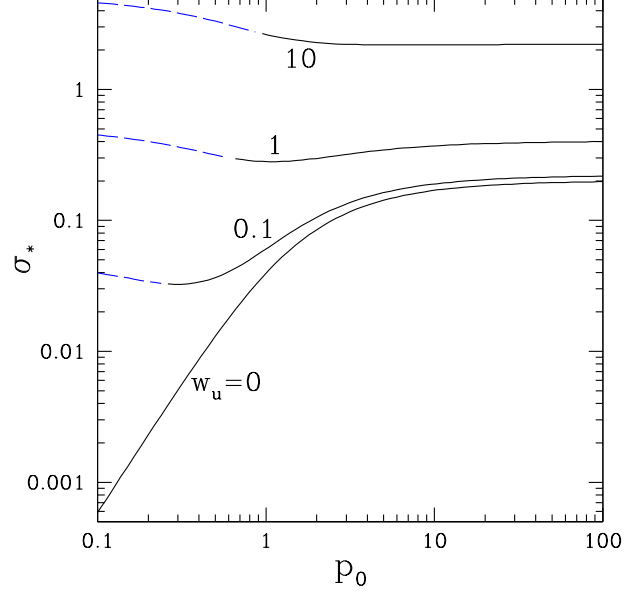


FIG. 6.— The characteristic upstream magnetization σ_* that gives $w_d/\sigma_d = 2$ in the downstream. A strong collisionless sub-shock should form in the RMS if $\sigma_u \gtrsim \sigma_*$. Each curve shows the dependence of σ_* on the shock strength p_0 for a fixed upstream enthalpy w_u (indicated next to the curve). The curves are dashed where the shock is weak, $v_0 < c_s$.

fine a characteristic magnetization $\sigma_u = \sigma_*$ such that a shock propagating in the medium will have $w_d/\sigma_d = 2$ (the boundary of the red-dotted region in Figure 5). The magnetization σ_* depends on the shock strength p_0 (upstream momentum measured in the downstream frame). This dependence is shown in Figure 6. In the ultra-relativistic limit $p_0 \gg 1$, we find that σ_* does not depend on p_0 (both w_d and σ_d scale as p_0^2 , so their ratio does not depend on p_0). For non-relativistic shocks $p_0 \ll 1$ with a cold upstream ($w_u = 0$), σ_* scales as p_0^2 . This is because weakly magnetized shocks have downstream enthalpy $w_d \propto p_0^2$ while $\sigma_d \propto \sigma_u$.

At large $\sigma > 1$ and $\sigma > w$, the effective sound speed c_s approaches the speed of light (see Equation 36). Shocks easily form if the internal compressive motions are supersonic, i.e. their Lorentz factors γ_0 exceed $\sigma^{1/2}$. The dissipation in magnetically dominated shocks occurs in a microscopically thin, collisionless shock front. Dissipation is reduced in this regime, as a large fraction of shock energy goes into the compressed magnetic field, however dissipation can still be significant. For example, a shock with Lorentz factor $\gamma_0 = 4$ propagating in a medium with upstream enthalpy $w = 1$ and $\sigma = 10$ has the downstream enthalpy $w_d \approx 6.8$ and $U_{\text{rad}} \approx 0.12 U_B$. In this example, the shock compression ratio is $\xi \approx 8.3$, and adiabatic compression would imply the amplification of w by only a factor of $\xi^{1/3} \approx 2$, well below 6.8. We note also that the downstream enthalpy w_d is mainly determined by the upstream enthalpy w_u and the amplitude of the shock; it weakly depends on σ_u .

4. SHOCKS IN PHOTON GAS

In GRB explosion models, sub-photospheric shocks begin to form at early stages, when the jet rest mass is still dominated by radiation, before the jet accelerates to its

asymptotic Lorentz factor. This section examines the structure of shock waves in this regime, neglecting magnetic fields.

In essence, we deal here with shocks in the gas of photons, as the plasma inertia is negligible. The plasma role is to provide opacity and thus to couple the photons into a single fluid, with a small mean free path. The plasma particles may be viewed as passive “markers” following the motion of the photon gas.

4.1. Jump conditions

Far upstream and far downstream of the shock, the radiation can be described as ideal fluid with isotropic pressure P and the stress-energy tensor

$$T^{\mu\nu} = 4P u^\mu u^\nu + P g^{\mu\nu}, \quad (44)$$

where we have used the equation of state $U = 3P$. Jump conditions express the continuity of T^{tx} (flux of energy) and T^{xx} (flux of momentum) in the rest frame of the shock,

$$4P_d \gamma_d^2 \beta_d = 4P_u \gamma_u^2 \beta_u, \quad (45)$$

$$4P_d \gamma_d^2 \beta_d^2 + P_d = 4P_u \gamma_u^2 \beta_u^2 + P_u, \quad (46)$$

where subscript “u” stands for upstream and “d” for downstream; pressure is measured in the fluid frame, and velocity is measured in the shock frame. Dividing Equations (45) and (46), one finds that β_u and β_d satisfy the condition

$$g(\beta_u) = g(\beta_d), \quad g(\beta) = \frac{1 + 3\beta^2}{\beta}. \quad (47)$$

Rewriting the definition of g as

$$3\beta^2 - g\beta + 1 = 0, \quad (48)$$

one can view β_u and β_d as the two roots of the quadratic equation, and hence they are related by

$$\beta_u \beta_d = \frac{1}{3}. \quad (49)$$

Since $\beta_u > \beta_d$, one concludes that $\beta_u > 3^{-1/2}$. This condition merely states that the shock moves supersonically relative to the upstream (recall that the sound speed is $c_0 = 3^{-1/2}c$). Using the relation (49) and Equation (45) or (46), one finds the pressure jump across the shock

$$\frac{P_d}{P_u} = 3\gamma_u^2 \left(\beta_u^2 - \frac{1}{9} \right). \quad (50)$$

The shock compresses the volume measured in the fluid frame by the factor

$$\xi = \frac{\gamma_u \beta_u}{\gamma_d \beta_d} = \gamma_u \beta_u (9\beta_u^2 - 1)^{1/2}, \quad (51)$$

which also gives the relation

$$\frac{P_d}{P_u} = \frac{\xi^2}{3\beta_u^2}. \quad (52)$$

For ultra-relativistic shocks, $\beta_u \rightarrow 1$, the jump conditions simplify to $\beta_d = 1/3$ and $P_d/P_u = (8/3)\gamma_u^2 = \xi^2/3$.

4.2. Evolution equation for the photon gas

Formation of shocks in the gas of photons can be simulated numerically. It is convenient to think of this problem as a radiative transfer problem for the bolometric intensity of radiation I . Since the stress-energy tensor is dominated by radiation, the plasma is effectively massless and its velocity β is controlled by the “force-free” condition: β equals the equilibrium value such that the radiation flux in the fluid frame vanishes (zero flux implies zero force applied by radiation to the plasma). This condition leads to a well-defined radiative transfer problem (Beloborodov 1999). It has a simple solution for steady spherically symmetric relativistic outflows (Beloborodov 2011). Here we are interested in shock formation in variable outflows, so the problem is time-dependent.

The shock is thin and locally flat (in the y - z plane), and we can study its formation in the plane-parallel geometry. Then the bolometric intensity is described by the function $I(t, x, \mu)$ where $\mu = \cos \theta$ and θ is the photon angle with respect to the x -axis.

The stress-energy tensor of radiation is determined by the moments of the intensity,

$$I_k(t, x) = \frac{1}{2} \int_{-1}^1 I(t, x, \mu) \mu^k d\mu. \quad (53)$$

In particular, $T^{tt} = 4\pi I_0$, $T^{tx} = 4\pi I_1$, and $T^{xx} = 4\pi I_2$. The force-free condition reads $\tilde{I}_1 = 0$ in the fluid frame, and the transformation of $T^{\mu\nu}$ from the lab frame to the fluid frame gives the quadratic equation for velocity,

$$\tilde{I}_1 = \gamma^2 [-\beta(I_0 + I_2) + (1 + \beta^2)I_1] = 0, \quad (54)$$

$$\Rightarrow \quad \beta = \zeta - (\zeta^2 - 1)^{1/2}, \quad \zeta \equiv \frac{I_0 + I_2}{I_1}. \quad (55)$$

The evolution of intensity is described by the transfer equation,

$$\frac{1}{c} \frac{\partial I}{\partial t} = -\mu \frac{\partial I}{\partial x} + n\sigma_T(1 - \beta\mu)(S - I), \quad (56)$$

where n is the number density of electrons/positrons measured in the lab frame, and S is the source function. In the simplest case of isotropic scattering, S is given by (Beloborodov 1999)

$$S(\mu) = \frac{I_0 - \beta I_1}{\gamma^4(1 - \beta\mu)^4}. \quad (57)$$

4.3. Numerical solution

Equation (56) supplemented with the equilibrium velocity condition (Equation 55) can be solved numerically. A sample solution is shown in Figure 7. In this example, the initial state is given by Equation (2) with $p_{\max} = 2$ and $L = 50$. The initial plasma density is uniform in the lab frame, $\rho(0, x) = \rho_0 = \text{const}$, and the unit length in x corresponds to a slab of unit Thomson optical depth. The initial radiation density measured in the fluid frame is uniform in the lab frame, $U(0, x) = U_0 = \text{const}$.

One can see the compression of the converging supersonic flow and the formation of a pair of shocks symmetric about $x = 0$, as described in Section 2. As the two shocks continue to propagate, the downstream fluid

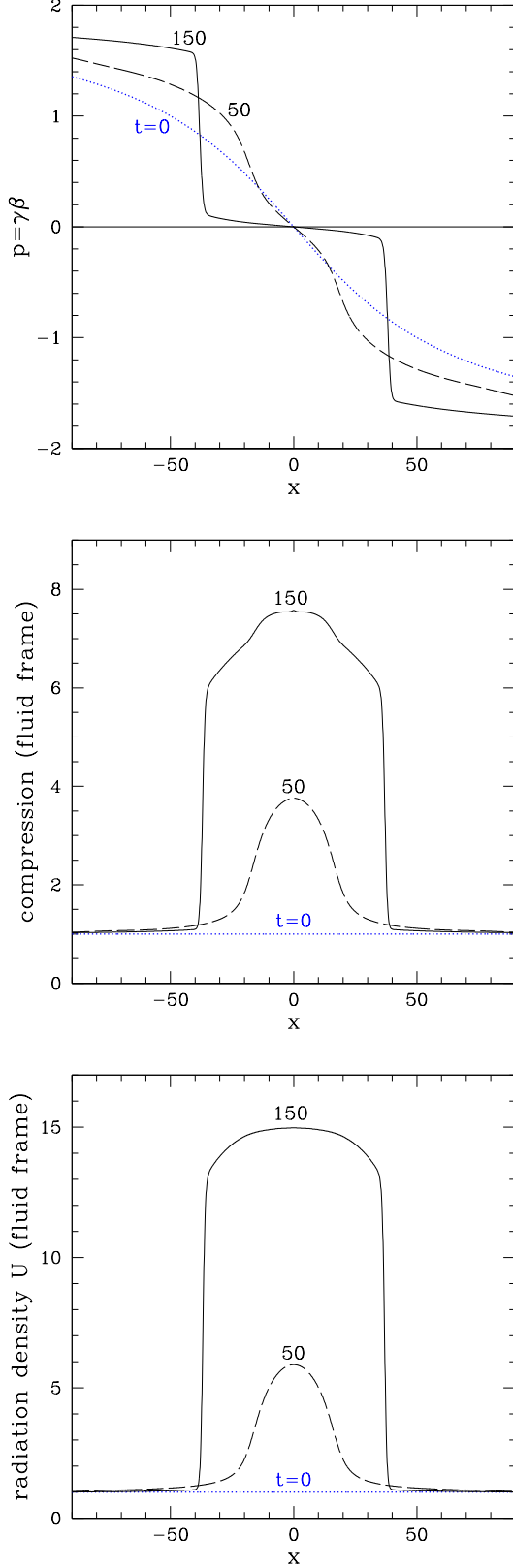


FIG. 7.— Evolution of the fluid velocity, compression, and radiation energy density U (measured in the fluid frame). Unit length in x corresponds to a slab of unit Thomson optical depth in the initial state. The indicated times are measured in units where $c = 1$.

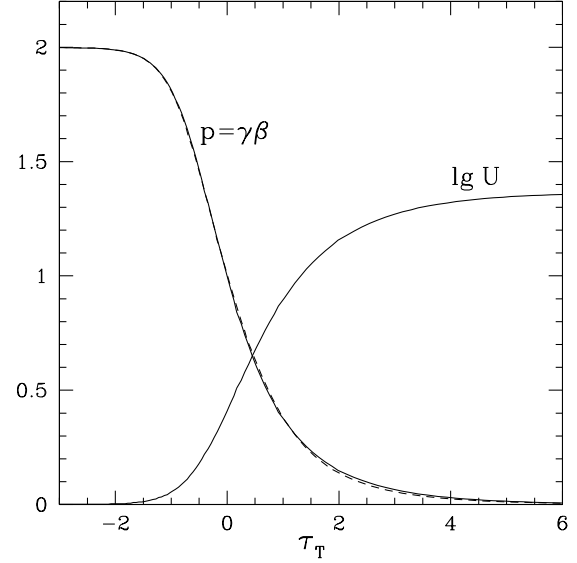


FIG. 8.— Shock wave in “photon gas” ($U_{\text{rad}} \gg \tilde{\rho}c^2, U_B$). The shock structure is shown as a function of Thomson optical depth τ_T in the frame where the downstream is at rest. The reference point $\tau_T = 0$ is chosen at half-maximum of the momentum profile $p = p_0/2$. Energy density $U = 4\pi\tilde{I}_0$ is measured in the fluid frame (normalized to its pre-shock value). The solid curves show the shock wave with amplitude $p_0 = 2$. The dashed curve shows $p(\tau_T)/2$ for the shock with $p_0 = 4$.

comes nearly to rest in the lab frame. The upstream velocity relative to the downstream, β_0 , is related to the upstream and downstream velocities measured in the shock frame by

$$\beta_0 = \frac{\beta_u - \beta_d}{1 - \beta_u \beta_d}. \quad (58)$$

Using $\beta_d \beta_u = 1/3$ (Section 4.1), one finds

$$\beta_u = \frac{1}{3} \left[\beta_0 + (\beta_0^2 + 3)^{1/2} \right]. \quad (59)$$

Once the shock wave is established, its structure becomes independent of the details of the initial conditions. The shock has only one parameter: β_0 or $p_0 = \gamma_0 \beta_0$. Figure 8 shows the obtained structure of a shock wave with $p_0 = 2$. It is shown as a function of the optical depth measured in the x direction. Then the result is independent of the plasma density, so the obtained solution is unique. Using $\beta_0 = 2^{-1/2}$ and $\beta_u = 0.7903$ that correspond to $p_0 = 2$, one finds from Equations (51) and (52) the ratio of downstream and upstream pressures $P_d/P_u = U_d/U_u = 23.3$. This asymptotic value of U is observed in Figure 8.

For comparison, Figure 8 also shows the momentum profile $p(x)$ for a shock with $p_0 = 4$, obtained from a similar time-dependent simulation. When re-scaled by the factor of 2, the momentum profile is the same as for $p_0 = 2$.

5. MONTE-CARLO SIMULATIONS OF SHOCKS

Time-dependent simulations may also be employed to study shocks in plasma with significant rest mass and magnetic fields. In contrast to the photon gas studied in Section 4, now the radiative transfer equation cannot

be closed by the force-free condition $\tilde{I}_1 = 0$. Instead, the fluid acceleration must be calculated together with the radiative transfer. Another complication is the need to follow the evolution of the radiation spectrum, which develops a hard tail extending above $\sim m_e c^2$ inside the shock front; then the scattering cross section is changed by the electron recoil.

Below we solve this problem using a direct numerical experiment that follows individual photons and their interactions with the plasma, so that the transfer of momentum and energy is described on a microscopic level. In the initial state, the flow has a smooth velocity profile described by Equation (2) and carries thermal radiation, which is isotropic in the fluid frame. The flow is opaque and supersonic, which leads to the formation of a pair of shocks propagating in the $\pm x$ directions, as described in Section 2.

The flow has two interacting components:

(1) Magnetized plasma. The plasma is assumed to carry a transverse magnetic field, which provides strong coupling between all charged particles, so their dynamics along the x axis is well described as a single-fluid motion.³ In the numerical simulations we use a Lagrangian grid moving together with the fluid of charged particles: the fluid is discretized into $N \sim 10^4$ shells of equal rest mass m and a small scattering optical depth. Besides mass, each shell is characterized by the magnetic flux frozen in it, internal thermal energy, and total pressure. The magnetic flux remains constant while thermodynamic quantities may change as the shell contracts (or expands) and interacts with radiation. Thermal conductivity of the plasma in the x -direction is suppressed by the transverse magnetic field and neglected.

(2) Radiation. Radiation is represented by $\sim 10^8$ photons which are followed individually. The photons migrate through the plasma shells and occasionally scatter off a thermal electron. The scattering is followed using Monte-Carlo technique, with the exact Klein-Nishina differential cross section and assuming that the thermal electrons are isotropic in the fluid frame. The electrons are assumed to have a Maxwellian distribution with a self-consistently calculated temperature.

A detailed description of the numerical method will be given in an upcoming paper. A possible alternative to the Monte-Carlo method is the solution of the transfer equation for the radiation intensity, as in Section 4 but now including fluid inertia. A similar approach was taken in the recent work by Ohsuga & Takahashi (2016) who simulated the evolution of bolometric intensity assuming Thomson scattering. Thomson approximation may be sufficient only for the RMS with negligible fluid inertia $\tilde{\rho}c^2 \ll U_{\text{rad}}$. If $\tilde{\rho}c^2 \gtrsim U_{\text{rad}}$, strong bulk Comptonization develops in the RMS and, if treated in the Thomson approximation, leads to runaway in photon energy (Blandford & Payne 1981). Scattering with substantial electron recoil, in the Klein-Nishina regime, becomes inevitable and limits the growth of photon energy. The electron recoil is also essential in maintaining heat exchange between radiation and plasma, even when the

photon energies (and the plasma temperature) are well below $m_e c^2$.

5.1. Sample models

In our two sample simulations the initial flow has dimensionless enthalpy $w = 0.1$ and magnetization $\sigma = 0$ (Model A) or $\sigma = 0.1$ (Model B). The initial average photon energy in the fluid frame is everywhere $3kT \approx 10^{-2}m_e c^2$. In both simulations we observed how the compressive wave with amplitude $p_{\text{max}} = 2$ steepened and formed a pair of shocks at time $t \approx L/c$. We chose a sufficiently large optical depth of the steepening region $\tau_L = \sigma_T n L = 20$ and observed how the magnetic field and the trapped radiation were advected toward $x = 0$, building up a strong pressure maximum. This launched the RMS, as described in Section 2, and the two symmetric shocks continued to propagate away from $x = 0$. The amplitude of the shocks p_0 slowly grows as they propagate toward the asymptotic momentum of the converging flow $p_{\text{max}} = 2$.

Figure 9 shows one of the two symmetric shocks at $t \sim 3L/c$ in Model A (upper panel) and Model B (lower panel). By this time the shock has crossed a Thomson optical depth $\tau_T \sim 60$ from its formation site, and the upstream momentum has reached $p_0 \approx 1.6$. The shock structure is steady and propagating relative to the downstream with speed $v \approx 0.3v_0$. The shock exhibits the jump conditions calculated in Section 3. In particular, the shock compression ratio in Model B is $\xi = \tilde{\rho}_d/\tilde{\rho}_u \approx 6.8$. The jump conditions also give a moderate ratio $\sigma_d/w_d \approx 0.6$; it turns out sufficient to form a strong collisionless subshock. The simulation confirms the expectation from Section 3 that the flow magnetization leads to a strong collisionless subshock in the RMS. The subshock becomes weak if the magnetization is reduced and disappears in Model A with $\sigma = 0$.

The observed shock structure in Model B ($\sigma = 0.1$) may be summarized as follows. The momentum profile $p(\tau_T)$ is shallow toward the upstream; this part is shaped by radiation pressure that gradually decelerates the upstream on a scale comparable to the photon mean free path ℓ_{ph} . The profile steeply drops toward the downstream and has a kink connecting to the flat $v \approx 0$. The steep drop is accompanied by a narrow and strong spike in the plasma temperature. It has a finite thickness in our simulation, because we employed a small viscosity to keep shocks resolved by the Lagrangian grid. The optical depth of the steep drop $\delta\tau_T \approx 0.2$ is sufficiently small to exclude its support by radiation diffusion. With reduced viscosity, the profile steepens even more and forms a discontinuous jump with $\delta\tau_T \approx 0$ — the collisionless subshock.

A large fraction of the subshock energy gets stored in the compressed magnetic field, and a fraction is dissipated into plasma heat, as required by the jump conditions. This heat adds to the RMS entropy generated by photon diffusion between the upstream and downstream. The viscous heating in the simulation occurs near the kink (where the second derivative of the velocity profile peaks) and gives a narrow temperature spike immediately behind the velocity jump — a stark signature of subshock dissipation. The high photon-to-electron ratio ($\sim 10^3$ in the simulation) results in fast electron cooling, on a timescale $t_{\text{IC}} \ll \ell_{\text{ph}}/c$. It forces the postshock tem-

³ For any realistic magnetic field the Larmor radii of ions and electrons are microscopic, many orders of magnitude smaller than the photon free path. Therefore, we assume strong magnetic coupling of the plasma particles even in the weakly magnetized model that is formally labeled as $\sigma = 0$.

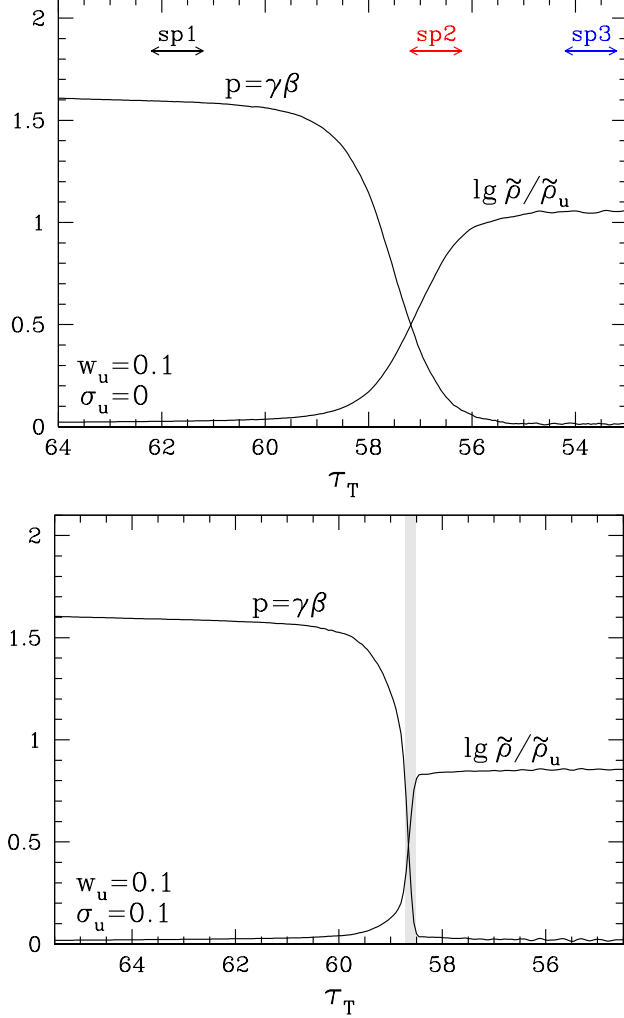


FIG. 9.— Snapshot of a shock propagating in the flow with upstream radiation enthalpy $w_u = 0.1$ and upstream magnetization $\sigma_u = 0$ (upper panel) or 0.1 (lower panel). The shock is propagating to the left and the Thomson optical depth τ_T is measured from the site of shock formation (caustic of the initial supersonic wave). The solid curves show the profiles of momentum $p = \gamma\beta$ and proper density $\tilde{\rho}$ (normalized to the upstream proper density $\tilde{\rho}_u$). A strong subshock has formed in the magnetized case; it is highlighted by the grey strip. The subshock is resolved (not a discontinuous jump) due to a finite viscosity employed in the simulation of plasma dynamics; the small subshock thickness $\delta\tau_T \approx 0.2$ is controlled by viscosity. Radiation is everywhere simulated directly as a large collection of individual photons whose propagation and scattering is followed using the Monte-Carlo technique. The photon spectra measured at three locations (indicated as sp1, sp2, sp3) are shown in Figure 10.

perature to quickly return to the Compton equilibrium with the local radiation field. Subshock cooling is accompanied by additional processes that will be discussed in Section 6 below.

The Monte-Carlo simulation provides photon statistics that show how the radiation spectrum evolves across the shock front. Figure 10 shows this evolution in the simpler case of $\sigma = 0$ where there is no subshock and no synchrotron emission. Then the spectrum is shaped by the bulk Comptonization effect, which was discussed previously (Blandford & Payne 1981; Levinson & Bromberg 2008): a fraction of photons cross the shock back and

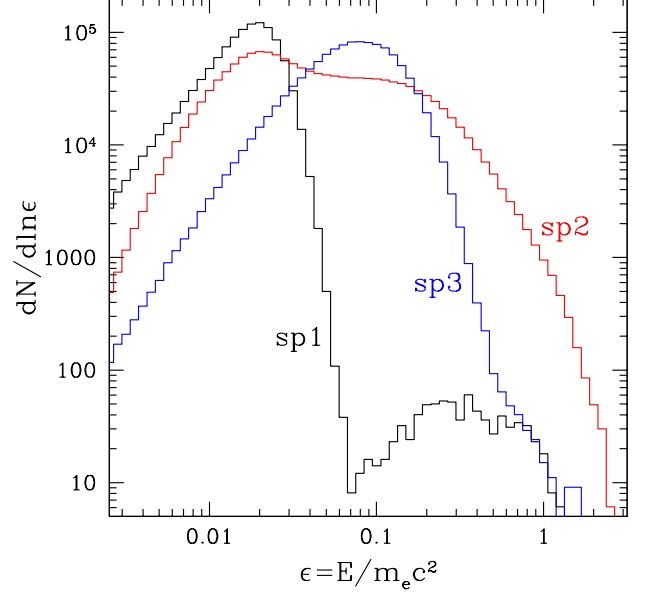


FIG. 10.— Photon spectrum $dN/d\ln E$ at three locations in Model A: upstream (black), in the middle of the shock (red), and downstream (blue); the three locations are indicated in Figure 9. Everywhere photon energy E is measured relative to the downstream frame. The overall scale on the vertical axis is arbitrary (it was chosen to reflect the photon number per energy bin used to construct the histogram). The shock has the upstream radiation enthalpy $w_u = 0.1$, magnetization $\sigma = 0$, and amplitude $p_0 = 1.6$. The snapshot of the simulation is taken at the same time as in Figure 9. The shock structure is nearly steady by this time, and the high-energy spectrum inside the RMS approaches saturation. The high-energy component seen in the upstream spectrum (the gamma-ray precursor) weakens with distance from the shock. The downstream spectrum is relaxing toward Compton equilibrium and reaches the Wien shape further downstream.

forth multiple times, with the energy boost $\sim \gamma_0^2$ in every cycle, similar to Fermi diffusive acceleration. As a result, the photon spectrum extends somewhat above $m_e c^2$ in the fluid frame. Further energy growth is hindered by downscattering due to the strong electron recoil (and also by photon conversion to e^\pm pairs, see below). At large optical depths downstream of the shock, the multiple downscattering of high-energy photons drives the spectrum toward a Wien shape in Compton equilibrium with the electrons.

5.2. Pair creation

Let us consider the weakly magnetized RMS, with no collisionless subshock. The ability of bulk Comptonization to generate photons with energies $E > m_e c^2 = 511$ keV in the fluid frame implies a significant rate of e^\pm pair creation due to reaction $\gamma + \gamma \rightarrow e^+ + e^-$. This reaction was not included in our Monte-Carlo simulations, and below we discuss its effect on the RMS structure.

The rate of pair creation can be estimated by noting that the absorbed MeV photons are replenished with rate $\sim n_1/t_1$ where $n_1 = dn_\gamma/d\ln E$ at $E = m_e c^2$ and $t_1 \sim (3 - 10)\ell_{ph}/c$ is the time it takes a 0.5-MeV photon to double its energy through bulk Comptonization. The radiation spectrum inside the RMS shows $n_1 \sim 10^{-2}n_\gamma$, where n_γ is the total photon density. Therefore, one can

roughly estimate the pair production rate as

$$\dot{n}_{\pm} \sim 10^{-3} \frac{cn_{\gamma}}{\ell_{\text{ph}}}. \quad (60)$$

Combining this with the characteristic timescale of the shock propagation, ℓ_{ph}/c , one obtains an order-of-magnitude estimate for the pair density in the RMS, $n_{\pm} \sim 10^{-3} n_{\gamma}$. The corresponding number of e^{\pm} created per proton is

$$Z_{\pm} \sim 10^{-3} \frac{n_{\gamma}}{n} = 10^2 \left(\frac{n_{\gamma}/n}{10^5} \right), \quad (61)$$

where $n_{\gamma}/n \sim 10^5$ is a typical photon-to-baryon ratio in GRBs.

This estimate neglects two effects, which somewhat reduce Z_{\pm} :

(1) Equation (61) assumes that the photons reaching ~ 1 MeV are quickly absorbed in γ - γ collisions, neglecting their finite free path. The MeV photons collide with each other, as they are near the threshold for γ - γ reaction, $2m_e c^2 \approx 1$ MeV. Their free path $\ell_{\gamma\gamma}$ may be estimated using the cross section for γ - γ collision $\sigma_{\gamma\gamma} \sim 0.1\sigma_{\text{T}}$. Then one finds $\ell_{\gamma\gamma} \sim 10(\sigma_{\text{T}}n_1)^{-1} \sim 10^3(Z_{\pm}n/n_{\gamma})\ell_{\text{ph}}$, and

$$\frac{\ell_{\gamma\gamma}}{\ell_{\text{ph}}} \sim \frac{Z_{\pm}}{10^2} \left(\frac{n_{\gamma}/n}{10^5} \right)^{-1} \sim 1. \quad (62)$$

Hence a large fraction of e^{\pm} creation occurs inside the RMS, as assumed in Equation (61), and so the finite $\ell_{\gamma\gamma}$ is not a big change.

(2) Equation (61) neglects the effect of e^{\pm} annihilation. The annihilation rate $\dot{n}_{\text{ann}} = (3/8)\sigma_{\text{T}}cn_{+}n_{-}$ implies a positron lifetime $t_{\text{ann}} = (8/3)(\sigma_{\text{T}}cn_{-})^{-1}$. The positrons are advected by the flow with a mildly relativistic speed and annihilate over a distance that corresponds to Thomson optical depth ~ 1 , comparable to the RMS thickness. Hence annihilation has a moderate reduction effect on Z_{\pm} inside the RMS.

These estimates show that Z_{\pm} inside the RMS can approach $\sim 10^2$. The exact value can be obtained from detailed numerical simulations and will depend on the upstream temperature, strength of the shock γ_0 , and n_{γ}/n . Z_{\pm} peaks inside the RMS and decreases with distance in the downstream, because of e^{\pm} annihilation.

The created mildly relativistic pairs are almost immediately cooled by inverse Compton (IC) emission and Coulomb collisions with the background plasma. The corresponding energy loss rates of an electron with Lorentz factor $\gamma_e = (1 - \beta_e^2)^{-1/2}$ are given by (e.g. Ginzburg & Syrovatskii 1964)

$$\dot{E}_{\text{IC}} \approx \frac{4}{3} \sigma_{\text{T}} U_{\text{rad}} \gamma_e^2 \beta_e^2, \quad (63)$$

$$\dot{E}_{\text{Coul}} \approx \frac{3 \ln \Lambda \sigma_{\text{T}} n_{\pm} m_e c^3}{2 \beta_e}, \quad (64)$$

where $\ln \Lambda = \ln(m_e c^2 / \hbar \omega_{\text{pl}}) \approx 20$ is a Coulomb logarithm (ω_{pl} is the Langmuir plasma frequency). Their ratio may be written as

$$\frac{\dot{E}_{\text{IC}}}{\dot{E}_{\text{Coul}}} \approx \frac{10^2}{Z_{\pm}} \frac{U_{\text{rad}}}{\bar{\rho} c^2} \gamma_e^2 \beta_e^3, \quad (65)$$

where $Z_{\pm} = n_{\pm}/n$ is the number of e^{\pm} per proton. For the typical parameters, the Coulomb losses dominate when $\gamma_e \beta_e \lesssim 1$. Thus the injected mildly relativistic particle shares a significant fraction of its energy with the background plasma and deposits momentum $\sim m_e c$. The estimated rate of γ - γ absorption then implies the force $f_{\text{abs}} \sim \dot{n}_{\pm} m_e c$ exerted on the plasma. This additional force is modest compared with the radiation pressure force $f_{\text{sc}} \sim \dot{n}_{\text{sc}} \epsilon_p m_e c$, where $\dot{n}_{\text{sc}} = \sigma_{\text{T}} c n_{\pm} n_{\gamma} = n_{\gamma} c / \ell_{\text{ph}}$ is the scattering rate and $\epsilon_p m_e c^2 \sim 10$ keV is the average photon energy. Using the above estimates one finds $f_{\text{abs}}/f_{\text{sc}} \sim \dot{n}_{\pm}/\dot{n}_{\text{sc}} \epsilon_p \lesssim 0.1$.

Pair creation increases the local scattering opacity $\kappa(x) = Z_{\pm}(x)\sigma_{\text{T}}/m_p$ by the factor Z_{\pm} . In essence, an additional e^{\pm} “screen” is created between the upstream and downstream. The thickness of a relativistic RMS is always a few ℓ_{ph} , and e^{\pm} loading implies that the RMS thickness shrinks proportionally to $\ell_{\text{ph}} = (n_{\pm}\sigma_{\text{T}})^{-1} \propto Z_{\pm}^{-1}$. For simplicity, the Monte-Carlo simulations presented in Section 5.1 assumed $\kappa = \text{const}$. This assumption is not important as long as (1) the shock structure is steady and (2) the velocity and density profiles of the shock wave are viewed as functions of the scattering optical depth (as in Figure 9) rather than the spatial coordinate x . In the plane-parallel approximation (valid when the RMS thickness is much smaller than its radius) the actual length ℓ_{ph} does not matter, and the optical depth is the natural coordinate.

6. COLLISIONLESS (SUB)SHOCK HEATING

In this section, $v_0 = \beta_0 c$ refers to the strength of the collisionless shock, which may be embedded in a stronger RMS. The shock thickness is microscopic, comparable to the ion Larmor radius.

The heat generated by the shock is initially given to the plasma particles and then converted to radiation, at some distance downstream of the shock. In particular, the post-shock ions receive thermal speeds $v_{\text{th}} \sim v_0$, as the shock thermalizes their upstream bulk speed v_0 . Numerical simulations of collisionless electron-ion shocks show that fast collective processes help the ions to promptly pass a fraction $f_e \sim 0.3 - 0.5$ of their energy to the electrons, and both form Maxwellian distributions (Sironi & Spitkovsky 2011).

The fraction f_e is less studied for the most interesting shocks in pair-loaded plasma, with $1 \ll Z_{\pm} \ll m_i/m_e$, where m_i is the ion mass. The existing work on pair-loaded shocks with transverse magnetic fields focused on the ultra-relativistic regime, with application to pulsar wind nebulae. It was found that such shocks are capable of positron acceleration through cyclotron maser instability of gyrating ions (Hoshino et al. 1992; Amato & Arons 2006; Stockem et al. 2012). It is unclear if particle acceleration may be efficient in moderately relativistic internal shocks in GRBs.

Below we discuss how the postshock plasma radiates its energy, assuming a two-temperature state. The electron and ion temperatures immediately behind the shock are controlled by the parameter f_e . The thermal Lorentz factor of the ions, γ_{th} , is related to the upstream Lorentz factor $\gamma_0 = (1 - \beta_0^2)^{-1/2}$ by

$$\gamma_{\text{th}} - 1 = (1 - f_e)(\gamma_0 - 1), \quad (\text{ions}). \quad (66)$$

The electrons are heated to much higher Lorentz factors,

$$\gamma_{\text{th,e}} = f_e(\gamma_0 - 1) \frac{m_i}{Z_{\pm} m_e} \gg 1, \quad (\text{electrons}), \quad (67)$$

where $Z_{\pm} = n_{\pm}/n$ is the number of e^{\pm} pairs per proton upstream of the collisionless shock. We will first discuss electron cooling and then ion cooling.

6.1. Electron cooling

The suddenly heated electrons lose their energy to inverse Compton (IC) scattering on a short timescale,

$$t_{\text{IC}} = \frac{3m_e c}{4\sigma_{\text{T}} f_{\text{KN}} U_{\text{rad}} \gamma_{\text{th,e}}}, \quad (68)$$

where the factor $f_{\text{KN}} < 1$ describes the Klein-Nishina correction to the Compton cooling rate. Even accounting for pair creation, the photon number in GRB jets exceeds the electron number by a large factor (3-5 orders of magnitude when the jet Lorentz factor saturates). Therefore, the electron cooling time t_{IC} is much shorter than the free-path time of photons to scattering, $t_{\text{IC}} \ll \ell_{\text{ph}}/c$. The electrons are also cooled by synchrotron losses on the timescale,

$$t_{\text{syn}} = \frac{3m_e c}{4\sigma_{\text{T}} U_B \gamma_{\text{th,e}}}. \quad (69)$$

It is shorter than t_{IC} if $U_B > f_{\text{KN}} U_{\text{rad}}$.

The maximum energy of IC photons is determined by $\gamma_{\text{th,e}}$, which depends on Z_{\pm} (Equation 67). IC photons with energies $E_{\text{IC}} \gg 1$ MeV are processed through e^{\pm} cascade into secondary e^{\pm} pairs and eventually into photons of energy $\lesssim 1$ MeV, which are capable of escaping $\gamma\text{-}\gamma$ absorption (Svensson 1987).⁴ As a result, most of e^{\pm} pairs are created in collisions between photons of energy $E_{\text{IC}} \sim 1$ MeV, not much above the $2m_e c^2$ threshold. The situation resembles that described in Section 5.2.

The multiplicity of pairs created per shock-heated electron, \mathcal{M}_{\pm} , is maximum if synchrotron losses are small $U_B \ll f_{\text{KN}} U_{\text{rad}}$; then it approaches $\mathcal{M}_{\pm} \sim 0.2\gamma_{\text{th,e}}$. If the magnetic energy is comparable to the radiation density, synchrotron losses become dominant. This significantly reduces the pair yield $Y = \mathcal{M}_{\pm}/\gamma_{\text{th,e}}$ (see Table 1 in Vurm et al. 2011).

The population of MeV photons with peak density n_{MeV} spreads from the collisionless shock over the characteristic distance of their self-destruction in $\gamma\gamma$ collisions,

$$\ell_{\gamma\gamma} \sim (\sigma_{\gamma\gamma} n_{\text{MeV}})^{-1}. \quad (70)$$

The number of MeV photons emitted per shock-heated electron approximately equals the number of pairs they produce, i.e. $\mathcal{M}_{\text{MeV}} \sim \mathcal{M}_{\pm}$.

The e^{\pm} density in the pair-creation region of size $\sim \ell_{\gamma\gamma}$ is somewhat reduced by the annihilation reaction with rate $\dot{n}_{\text{ann}} = (3/8)\sigma_{\text{T}} c n_+ n_-$. The downstream evolution of the positron density n_+ is described by the equation,

$$v_d \frac{dn_+}{dx} = \dot{n}_{\gamma\gamma} - \frac{3}{8} \sigma_{\text{T}} c n_+ n_-. \quad (71)$$

⁴ Photons of energy E_{IC} are absorbed in collisions with photons of energies $E_t \gtrsim 2m_e^2 c^4 / E_{\text{IC}}$ with cross section $\sigma_{\gamma\gamma} \sim 0.1\sigma_{\text{T}}$. The mean free path to absorption is $\ell_{\gamma\gamma} = (\sigma_{\gamma\gamma} n_t)^{-1}$ where n_t is the target photon density. For instance, 100-MeV photons are absorbed by the Wien peak of the radiation spectrum ($E_t \sim 10$ keV in the fluid frame) and their $\ell_{\gamma\gamma} \sim 10(\sigma_{\text{T}} n_{\gamma})^{-1}$ is tiny.

Here $\dot{n}_{\gamma\gamma} \sim \sigma_{\gamma\gamma} c n_{\text{MeV}}^2$ is the pair creation rate, and $v_d \approx v_0/3$ is the velocity of the downstream relative to the collisionless shock.⁵ The advection rate across the pair-creation zone $v_d dn_+/dx \sim n_+ v_d / \ell_{\gamma\gamma}$ is comparable to or smaller than the terms on the right side of Equation (71). Therefore, the pair density is not far from the annihilation balance, $(3/8)\sigma_{\text{T}} c n_+ n_- \sim \sigma_{\gamma\gamma} c n_{\text{MeV}}^2$. This is still consistent with the crude estimate for the positron density $n_+ \sim n_{\text{MeV}}$, which determines the Thomson optical depth of the pair creation zone,

$$n_+ \sim n_{\text{MeV}}, \quad \tau_{\text{T}} \sim \sigma_{\text{T}} n_{\pm} \ell_{\gamma\gamma} \sim 2, \quad (72)$$

The production of MeV photons that convert to pairs is different from the RMS bulk Comptonization discussed in Section 5. However, it gives an optical depth comparable to that of an RMS.

6.2. Pair breeding upstream of collisionless shocks

The strong electron heating in collisionless shocks results in the MeV emission downstream of the shock, however some of the MeV photons can convert to pairs in the upstream. This leads to a special type of self-sustained breeding of pairs upstream of the shock.

The number of e^+ and e^- created per shock-heated electron may be written as $\mathcal{M}_{\pm} = \mathcal{M}_u + \mathcal{M}_d$ — the sum of e^{\pm} created upstream and downstream. Most of the pair-creating MeV photons are emitted relatively close to the collisionless shock, at a distance smaller than their absorption free-path $\ell_{\gamma\gamma}$.⁶ Therefore, IC photons emitted toward the upstream can overtake the shock and convert to pairs ahead of it.

A rough estimate for $\mathcal{M}_u/\mathcal{M}_{\pm}$ may be obtained assuming that the IC photons are emitted isotropically in the downstream fluid frame and that photons emitted with angles $\cos\theta > \beta_d$ (catching up with the shock) have a sufficiently long $\ell_{\gamma\gamma}$ to overtake the shock. Then,

$$\mathcal{M}_u \sim \frac{(1 - \beta_d)}{2} \mathcal{M}_{\pm}. \quad (73)$$

A more accurate value for \mathcal{M}_u may be found from Monte-Carlo transfer simulations. It will be somewhat below the estimate given in Equation (73).

\mathcal{M}_u particles are injected into the upstream per one electron (or positron) heated in the shock. They join the upstream, cool down, and then go through the shock like the primary electron did, closing the cycle. This cycle allows the upstream e^{\pm} population to reproduce itself with the amplification factor $\mathcal{M}_u > 1$.

⁵ The relation $v_d \approx v_0/3$ holds for plasma-mediated shocks with any amplitude v_0 , relativistic or non-relativistic, as long as the shock is strong (v_0 is much greater than the upstream thermal speed). The relation $v_d = v_0/3$ is derived analytically from the jump conditions in the “monoenergetic gas” approximation (Beloborodov & Uhm 2006).

⁶ In a GRB jet, the average photon energy in the fluid frame is comparable to 10 keV. Most of the pair-creating IC photons are generated in the Thomson regime, $E_{\text{IC}} \sim \gamma_e^2 \times 10$ keV, by e^{\pm} with $\gamma_e \lesssim 30$ over length $\ell_{\text{IC}} \approx v_d t_{\text{IC}} \sim 0.1\beta_d m_e c^2 / \sigma_{\text{T}} U_{\text{rad}}$, cf. Equation (68). The length ℓ_{IC} is much shorter than $\ell_{\gamma\gamma}(E_{\text{IC}})$. If pair creation involves a cascade with multiple generations, many of the electrons with $\gamma_e < 30$ would be secondary and injected over an extended length due to the intermediate steps of $\gamma\text{-}\gamma$ absorption. However, even in this case the additional steps are relatively short, as $\ell_{\gamma\gamma}(100 \text{ MeV}) \ll \ell_{\gamma\gamma}(10 \text{ MeV}) \ll \ell_{\gamma\gamma}(1 \text{ MeV})$.

The breeding of upstream pairs is, however, limited, because $\gamma_{\text{th},e} \propto Z_{\pm}^{-1}$. The increasing upstream Z_{\pm} eventually reduces $\gamma_{\text{th},e}$ to γ_{cr} that is marginally sufficient for production of IC photons capable of converting ahead of the shock. Then a self-consistent situation is achieved with $\mathcal{M}_u \approx 1$ — the upstream pair population is replenished with no further growth. The pair loading factor ahead of the shock is then given by

$$Z_{\pm} \approx f_e(\gamma_0 - 1) \frac{m_p}{\gamma_{\text{cr}} m_e} \sim 10^2 f_e \left(\frac{\gamma_{\text{cr}}}{20} \right)^{-1} (\gamma_0 - 1). \quad (74)$$

The critical value of $\gamma_{\text{th},e}$ can be estimated for a typical spectrum of radiation carried by GRB jets, which peaks around 10 keV in the fluid frame. Then $\gamma_{\text{cr}} \sim 20$ is capable of producing a large number of IC photons with $E_{\text{IC}} \gtrsim 3$ MeV.

The reduction of $\gamma_{\text{th},e}$ to γ_{cr} implies that the downstream e^{\pm} cascade has only one generation and a modest multiplicity $\mathcal{M}_{\pm} \sim 3$ -5. The downstream pair loading factor is much higher, $Z_{\pm} \gg \mathcal{M}_{\pm}$, due to the breeding of pairs ahead of the shock.

In an RMS, with or without a collisionless subshock, the upstream is decelerated by scattering the radiation flux from the downstream. The absorption of MeV photons implies an additional deceleration effect. It involves the upstream deposition of momentum $\sim Z_{\pm} m_e c$ per ion, which may approach ~ 0.1 of the ion momentum and is insufficient to significantly change the velocity profile of the shock wave.

This situation is in contrast with the previously studied e^{\pm} creation ahead of *external* blast waves from GRB explosions (Thompson & Madau 2000; Beloborodov 2002). In that case, the shock is driven by ultra-relativistic ejecta into a low density ambient medium of rest-mass $m c^2 \sim E_{\text{ej}}/\Gamma^2$, where E_{ej} is the explosion energy. The average GRB photon propagating ahead of the shock has energy comparable to 1 MeV in the rest frame of the ambient medium. Then the impact of pair creation and radiation pressure on the external medium is huge. The MeV radiation front is capable of sweeping up the external medium and even clearing a vacuum cavity ahead of the ejecta (Beloborodov 2002). Such effects cannot occur in internal shocks because they are much weaker and involve a much lower contrast in density.

6.3. Energy runaway?

Pair breeding described above involves electrons and photons of MeV energies and does not generate very high-energy particles. The most energetic particles have Lorentz factors $\sim \gamma_{\text{cr}}$ immediately behind the collisionless shock, and e^{\pm} pairs injected into the upstream have mildly relativistic $\gamma_e \sim 2$. Before reaching the collisionless shock, these pairs lose energy through Coulomb collisions with the background plasma and IC cooling (synchrotron cooling of mildly relativistic electrons is suppressed by self-absorption). Compton cooling results from scattering of background photons of energies $E_t < 100$ keV, and hence the upstream produces IC photons with energies $E_{\text{IC}} \sim \gamma_e^2 E_t < m_e c^2$. Thus, MeV radiation is only generated immediately behind the collisionless shock, with no amplification cycle in photon energy.

The situation could, however, change if the shock is

ultra-relativistic, $\gamma_0 \gg 1$. Then pair breeding occurs with a high energy gain per cycle, tapping into the kinetic energy of upstream motion relative to downstream. It can lead to a runaway cycle of photon energy boosting, which was noticed and described as “converter mechanism” by Derishev et al. (2003) and “electromagnetic catastrophe” by Stern (2003). The cycle involves IC emission followed by photon propagation across the collisionless shock, e^{\pm} creation on the other side, and IC emission from the created pair back toward the downstream. This effectively implies an exchange of IC photons between the upstream and downstream accompanied by the energy boost $\sim \gamma_0^2$. The runaway occurs if the cycle is closed with the mean expectation for the final photon energy exceeding the initial photon energy.

Consider an initial IC photon of energy $\epsilon_1 m_e c^2$ in the downstream frame, and suppose the photon overtakes the shock and converts to an e^{\pm} pair. The created particles have Lorentz factors $\gamma_e \sim \gamma_0 \epsilon_1 / 2$ in the upstream frame, and cool in the Klein-Nishina regime if $\gamma_e \epsilon_p \gtrsim 1$ (where $\epsilon_p m_e c^2 \sim 10$ keV describes the peak of radiation spectrum in the fluid frame). Then the new IC photons emitted by the e^{\pm} pair and viewed from the downstream frame have energies $\epsilon_2 \sim \gamma_0 \gamma_e / 2 \sim (\gamma_0^2 / 4) \epsilon_1$. The cycle is completed when the photon ϵ_2 propagates into the downstream, creates a pair with $\gamma_e \sim \epsilon_2 / 2$, and this pair produces IC photons with $\epsilon_f \sim \gamma_e / 2 \sim (\gamma_0 / 4)^2 \epsilon_1$. This rough estimate suggests that a runaway cycle, $\epsilon_f > \epsilon_1$, requires $\gamma_0 > 4$. It also requires two other conditions:

- (1) The electron cooling free path ℓ_{IC} should not exceed the free path of photons it produces, $\ell_{\gamma\gamma}$; otherwise the IC photon is absorbed before it has a chance to cross the shock. This condition is not satisfied for high-energy IC photons, $\epsilon \gg \epsilon_p^{-1}$, if the target radiation spectrum at $\epsilon_t < \epsilon_p$ has the photon index $\alpha = d \ln n_t / d \ln \epsilon_t < 0$. If $\alpha > 0$, IC scattering and γ - γ absorption of photons $\epsilon > \epsilon_p^{-1}$ involve the same main targets $\epsilon_t \sim \epsilon_p$ with comparable cross sections $\sigma_{\gamma\gamma} \sim \sigma_{\text{IC}} \sim (\epsilon \epsilon_p)^{-1} \sigma_{\text{T}}$; then $\ell_{\text{IC}} \sim \ell_{\gamma\gamma}$.
- (2) The magnetic fields should be weak; otherwise synchrotron losses become increasingly dominant over IC emission in the deep Klein-Nishina regime and suppress the production of high-energy IC photons.

In summary, the runaway of photons with growing energies requires an ultra-relativistic collisionless shock and weak magnetic fields. This combination is unlikely at large optical depths where the formation of strong collisionless shocks requires strong magnetic fields.

6.4. Ion cooling

The energy fraction kept by the ions behind the collisionless shock, $1 - f_e$, is not easily radiated — an ion cannot directly radiate its energy, because of its large mass m_i . The ions gradually lose their energy through Coulomb collisions with e^{\pm} or through nuclear collisions. Both processes are relatively slow, and the ion cooling can be a bottleneck for postshock heat conversion to radiation.

The e^{\pm} plasma behind the shock quickly becomes much colder than the ions. Frequent Compton scattering enforces kinetic equilibrium of electrons (and positrons) with local radiation at the Compton temperature $kT_C \sim 10$ –50 keV, which corresponds to a thermal speed around

0.3c. In the first approximation, the hot, mildly relativistic ions behind the collisionless shock view electrons as targets at rest, and the ion cooling timescale due to Coulomb collisions is approximately given by (e.g. Ginzburg & Syrovatskii 1964),

$$t_{\text{Coul}} = \frac{(\gamma_{\text{th}} - 1)m_i c^2}{\dot{E}_{\text{Coul}}} = \frac{2\beta_{\text{th}}(\gamma_{\text{th}} - 1)m_i}{3 \ln \Lambda \sigma_T n_{\pm} m_e c}, \quad (75)$$

where n_{\pm} is the local density of electrons and positrons and $\ln \Lambda \approx 20$ is the Coulomb logarithm.

During time t_{Coul} , the hot ions are advected through the distance

$$l_{\text{Coul}} = v_d t_{\text{Coul}} = \frac{v_0}{3} t_{\text{Coul}}, \quad (76)$$

where $v_d \approx v_0/3$ is the velocity of the downstream relative to the collisionless jump. The Thomson optical depth of the ion cooling region is

$$\tau_T = \sigma_T n_{\pm} l_{\text{Coul}} = \frac{2m_i \beta_0 \beta_{\text{th}} (\gamma_{\text{th}} - 1)}{9m_e \ln \Lambda}. \quad (77)$$

A significant fraction of radiation produced by the ion cooling at distance l_{Coul} behind the shock can diffuse back into the upstream if $\tau_T v_d/c \lesssim 1$. Otherwise, radiation is trapped and advected away from the shock, missing the chance to affect the upstream velocity profile. We conclude that the ion heat produced by the collisionless jump is effectively lost for the RMS if

$$\frac{2m_i \beta_0^2 \beta_{\text{th}} (\gamma_{\text{th}} - 1)}{27m_e \ln \Lambda} > 1. \quad (78)$$

This condition is satisfied for collisionless jumps with amplitude $p_0 = \gamma_0 \beta_0 \gtrsim 1$. In this case, the delay in ion cooling tends to reduce the radiative precursor and increase the amplitude of the collisionless jump.

The mildly relativistic ion (proton) temperature behind a strong subshock, $kT_i \sim 1$ GeV, leads to inelastic nuclear collisions between the protons, producing pions. Half of the pion energy is lost to neutrino emission while the other half is converted to e^{\pm} with Lorentz factors $\gamma_e \approx m_{\pi}/m_e \sim 300$. This injection of relativistic pairs by p-p collisions sustains an e^{\pm} cascade in the downstream region of thickness l_{Coul} . The cascade is similar to that triggered by inelastic n-p or n-n collisions in a neutron-loaded jet (Derishev et al. 1999; Beloborodov 2010).

The timescale for inelastic p-p collisions is $t_{pp} \approx (cn_p \sigma_{\text{inel}})^{-1}$ where $\sigma_{\text{inel}} = f_{\text{inel}} \sigma_n$ is a substantial fraction of the nuclear cross section $\sigma_n \approx \sigma_T/20$. The ion heat lost to inelastic collisions before it is given to e^{\pm} via Coulomb collisions is determined by the ratio

$$\frac{t_{\text{Coul}}}{t_{pp}} = \frac{2\beta_{\text{th}}(\gamma_{\text{th}} - 1)m_i \sigma_{\text{inel}}}{3 \ln \Lambda Z_{\pm} m_e \sigma_T} \sim \frac{1}{Z_{\pm}}. \quad (79)$$

One can see that e^{\pm} loading reduces the role of p-p collisions behind the shock.

7. TRANSFORMATION OF SHOCKS NEAR PHOTOSPHERE

As an RMS emerges from the photosphere of the outflow, it must transform into a pure collisionless shock: radiation becomes decoupled from the plasma and the

shock must be sustained by collective (collisionless) plasma processes. This transformation occurs through the growth of the collisionless subshock inside the RMS.

A key feature described in Sections 5.2 and 6 is that the shocks are dressed in e^{\pm} pairs. This delays their transition to transparency and thus delays the transition to a pure collisionless state. While the upstream and far downstream regions are already transparent to radiation, the shock itself remains opaque until its pair dress becomes optically thin. The estimated pair-loading factor Z_{\pm} inside the shock front is comparable to 10^2 , and hence the effective photospheric radius should be increased by a factor $\sim 10^2$. The shock “carries” the photosphere with it and keeps radiating right at the photosphere rather than crosses it.

Pair creation is strong even before the shock approaches the photosphere. A weakly magnetized relativistic shock generates pairs through bulk Comptonization, as described in Section 5.2. In the magnetized case, pairs are generated by the collisionless subshock, as described in Section 6. In any case, when the shock attempts to emerge from the photosphere and become a pure collisionless jump, pair creation with a large Z_{\pm} is inevitable.

Details of the photospheric transition depend on the shock amplitude $p_0 = \gamma_0 \beta_0$ and magnetization σ . The radius R_{\star}^{\pm} where the shock eventually becomes transparent satisfies the condition $R_{\star}^{\pm} \sim Z_{\pm} R_{\star}$ where R_{\star} is the photosphere in the absence of pair creation. Note that our estimates for Z_{\pm} assumed that most MeV photons ($\sim \Gamma \times \text{MeV}$ in the lab frame) emitted by the shock at a radius r convert to pairs with a free path $\ll r$ in the lab frame, which corresponds to $\ell_{\gamma\gamma} \ll r/\Gamma$ in the fluid frame. Taking into account that $\sigma_{\gamma\gamma} \sim 0.1\sigma_T$, this requires a sufficiently large “compactness” parameter,

$$l = \frac{U_{\text{rad}}}{m_e c^2} \sigma_T \frac{r}{\Gamma} \gg 10, \quad (80)$$

where $U_{\text{rad}} = L_{\text{rad}}/4\pi r^2 c \Gamma^2$ is the radiation energy density in the fluid frame and L_{rad} is the isotropic equivalent of the observed GRB luminosity. The compactness parameter is related to the characteristic Thomson optical depth of the outflow $\tau_T = n_{\pm} \sigma_T r / \Gamma$,

$$l \sim \frac{n_{\gamma}}{Z_{\pm} n} \frac{\bar{E}}{\Gamma m_e c^2} \tau_T \sim \frac{10^3}{Z_{\pm}} \tau_T, \quad (81)$$

where $\bar{E} \sim 1$ MeV is the average photon energy measured in the static lab frame, and $n_{\gamma}/n \sim 10^5$ is the typical photon-to-baryon ratio (we use the numerical values typical for GRBs). If $l \lesssim 10 - 30$, the $\Gamma \times \text{MeV}$ photons do not convert to pairs; only photons of significantly higher energies are quickly absorbed. A rough estimate for R_{\star}^{\pm} may be obtained by combining Equations (74) and (81), which gives $R_{\star}^{\pm} \sim 30 R_{\star}$. Its exact value depends on the parameters of the explosion.

A moderate magnetization of the flow $\sigma \sim 0.1$ implies that the collisionless shock expanding from R_{\star} to R_{\star}^{\pm} is a strong source of synchrotron photons. Unlike the IC photons (many of which convert to pairs) the synchrotron photons are soft and dominate the low-energy part of the shock radiation spectrum. Overall, the photospheric radiation released by the e^{\pm} -dressed shock should have a broad nonthermal spectrum around $\bar{E} \sim 1$ MeV

in the lab frame. It extends from the synchrotron self-absorption energy (well below 1 MeV) to the GeV break shaped by γ - γ absorption.

Detailed calculations of the emitted spectrum are deferred to a future paper. Here we note that the structure and observational appearance of the shock emerging from R_* is affected by the development of radiation anisotropy in the fluid frame. In any relativistic outflow, radiation develops a strong forward beaming in the fluid frame at optical depths $\tau_T \lesssim 10$ (Beloborodov 2011). As the e^\pm -dressed shock expands from R_* to R_*^\pm , its radiation maintains a strong beaming. This effect breaks the symmetry between shocks propagating forward and backward relative to the plasma outflow (shocks form in pairs propagating in the opposite directions relative to the fluid, see Section 2). The downstream of a backward internal shock is radially ahead of the upstream; hence the forward beaming reduces the efficiency of radiation diffusion from downstream to the upstream. This accelerates the development of the collisionless shock and also influences the effective optical depth τ_T of the e^\pm dress. In contrast, for a forward-propagating shock the downstream is radially behind the upstream. Then beaming assists sending photons into the upstream with a decreasing angle relative to the radial direction.

8. NUCLEAR COLLISIONAL DISSIPATION

8.1. Neutral particles in sub-photospheric shocks

In general, shock formation occurs when the steepening of the compressive wave is stopped by momentum (or heat) transfer due to the finite mean free path of particles. In a multi-component fluid, the importance of different components for the shock structure is determined by their contributions to viscosity and thermal conductivity. Both are controlled by the diffusion coefficient,

$$D = \frac{1}{3} \ell \bar{v}, \quad (82)$$

where ℓ is the mean free path and \bar{v} is the characteristic thermal speed of a given species of particles. In particular, the viscosity coefficient created by each species may be estimated as

$$\mu = D \xi \frac{H}{c^2}, \quad (83)$$

where ξ is the fractional contribution of the species to the relativistic enthalpy density of the flow H , which includes the rest-mass energy (H/c^2 serves as the effective inertial mass density in relativistic hydrodynamics).

Consider now shock formation deep below the photosphere. A simple comparison of viscosity coefficients of different components of the preshock flow allows one to judge their importance for the shock structure. In a first approximation, electrons, positrons, ions, and magnetic fields, move together as a single, strongly coupled fluid. In contrast, neutral particles — photons and especially neutrons — have large free paths and a large diffusion coefficient which leads to significant transfer of momentum and energy between the upstream and downstream, shaping the profile of the shock wave.

The consideration of diffusion coefficients assumes that the particles are not decoupled from the flow, i.e. their mean free-path time ℓ/\bar{v} is smaller than the age of the flow (measured in its rest frame). Neutrinos may carry

a significant fraction of the flow energy in GRBs, however they escape freely and do not contribute to viscosity. Photons contribute to viscosity at radii $r \lesssim R_*$ and neutrons — at radii $r \lesssim R_n$ where $R_n \approx R_*(\sigma_n/Z_\pm \sigma_T)$ is the neutron decoupling radius.

8.2. Neutron-mediated shock wave

GRB jets are expected to carry a significant number of free neutrons (Derishev et al. 1999; Beloborodov 2003). Their β -decay is delayed proportionally to the outflow Lorentz factor Γ and occurs at a characteristic radius $R_\beta \approx 8 \times 10^{15} (\Gamma/300)$ cm, which is much larger than the typical photospheric radius $R_* \sim 10^{12} - 10^{13}$ cm. Neutrons are coupled to the plasma through nuclear collisions with cross section $\sigma_n \approx 3 \times 10^{-26}$ cm², which is 20 times smaller than Thomson cross section. Neutrons have the largest mean free path, carry a significant fraction of the flow momentum, and hence can dominate the flow viscosity, affecting the formation of shocks. Neutron migration across the shock assist the momentum exchange between the upstream and downstream on a scale comparable to the neutron mean free path ℓ_n , shaping a broad, “neutron-mediated” shock wave.

This wave can have a strong subshock mediated by radiation, as the neutron collisions alone are unable to stop everywhere the velocity profile from steepening. If the neutron fraction of the outflow momentum is modest, the main momentum jump in the wave occurs in the subshock. Then the wave is better described as an RMS with a neutron precursor rather than a neutron-mediated shock. The RMS itself can have a strong collisionless subshock, depending on the flow magnetization. The resulting wave structure is schematically shown in Figure 11.

8.3. Nuclear collisions around RMS

Let us first consider small radii where the outflow rest-mass energy is dominated by radiation, $U_{\text{rad}} \gg \tilde{\rho} c^2$. Then the energy of neutrons (including their rest mass) is small compared with the energy dissipated in the RMS. The RMS thickness l_{sh} is comparable to the photon mean free path ℓ_{ph} . It is much smaller than the neutron mean free path ℓ_n ,

$$\frac{\ell_n}{\ell_{\text{ph}}} \sim Z_\pm \frac{\sigma_T}{\sigma_n} \approx 20 Z_\pm, \quad (84)$$

where $Z_\pm = n_\pm/n \geq 1$ determines the reduction of the photon free path in the plasma enriched by e^\pm pairs.

Neutrons brought by the upstream view the RMS as a discontinuity in the fluid velocity profile. They cross it ballistically and dissipate their energy $(\gamma_0 - 1)m_n c^2$ and momentum $p_0 m_n c$ at the characteristic distance $\sim \ell_n$ downstream of the shock. Their collisions with the downstream nuclear matter create a relativistically “hot” neutron (and ion) component embedded in the photon gas. Some of the hot neutrons propagate back into the upstream and collide there. They form a precursor of the shock — a “neutron pillow” that somewhat decelerates the upstream and thus reduces the strength of the RMS.

As long as neutron rest-mass density $\tilde{\rho}_n c^2$ is small compared with the enthalpy of the upstream photon gas, $4P_0$, the effect of neutron transport on the RMS amplitude is small. For example, consider a radiation-dominated jet

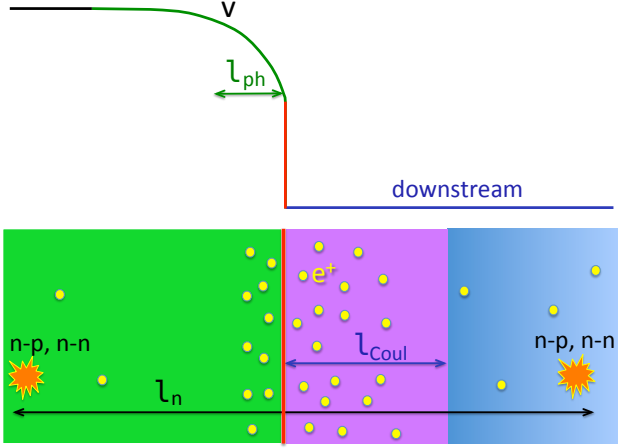


FIG. 11.— Structure of a relativistic internal shock in a hot, opaque, magnetized outflow. The green part of the velocity profile is shaped by the radiation pressure on a scale comparable to the photon mean free path to scattering ℓ_{ph} . The vertical red part is the collisionless subshock, which heats ions to a mildly relativistic temperature and electrons to an ultra-relativistic temperature (Section 6). The ultra-relativistic electrons are quickly cooled, producing synchrotron and IC photons, which create e^\pm pairs ahead and behind the shock. The ion cooling occurs on a longer scale ℓ_{Coul} , which may exceed the RMS thickness if the subshock is relativistic. Some of the hot ions experience inelastic p-p collisions before cooling. In the presence of a free neutron component in the flow, the shock wave is partially shaped by neutron migration between the upstream and downstream. The mean neutron free path ℓ_n is the longest scale in the shock structure. The migrating neutrons are stopped by nuclear collisions. Inelastic nuclear collisions result in injection of e^\pm with Lorentz factors $\gamma_e \sim m_\pi/m_e \sim 300$, distributed over a broad region $\sim \ell_n$. The nuclear collisions also emit neutrinos with observed energies $\sim \Gamma m_\pi c^2$ where Γ is the outflow Lorentz factor.

with an asymptotic (saturation) Lorentz factor Γ_{sat} at a small radius where the Lorentz factor is $\Gamma = 0.2\Gamma_{sat}$. At this early stage, 80% of the jet energy is carried by radiation, and about 20% is carried by baryons (neglecting here the energy of the magnetic field and e^\pm). Assuming that half of baryons are neutrons, one can estimate $\tilde{\rho}_n c^2 / 4P_0 \sim 0.1$, so roughly 10% of the shock energy is dissipated by nuclear collisions in this example. This dissipation occurs in the region of thickness $\sim \ell_n$ around the RMS. Even the modest amount of collisional dissipation at small radii (large optical depths) is important because it efficiently generates photons, as discussed below.

As the expanding and accelerating outflow experiences adiabatic cooling, the ratio $\tilde{\rho}_n c^2 / 4P_0$ increases and the role of collisional dissipation grows. When the Lorentz factor Γ approaches its maximum value Γ_{sat} , i.e. when radiation density U_{rad} becomes comparable to $\tilde{\rho} c^2$, a large fraction of the shock energy becomes dissipated through nuclear collisions. The wave front of thickness $\sim \ell_n$ — the neutron-mediated shock wave — propagates as long as the flow is opaque to nuclear collisions. When the wave approaches the neutron decoupling radius R_n the subshock (RMS) grows, and at larger radii $r > R_n$ the fraction of energy dissipation through nuclear collisions is reduced as R_n/r .

The RMS itself is not capable of producing ultra-

relativistic particles, and so collisional dissipation around the RMS plays a key role in this respect. Even in moderately relativistic shocks the neutron collisions are energetic enough to be inelastic. Such collisions produce mildly relativistic pions which quickly decay into ultra-relativistic e^\pm with Lorentz factors $\gamma_e \sim m_\pi/m_e$ (Derishev et al. 1999). This generates an inverse Compton cascade which produces copious e^\pm pairs. The resulting pair loading factor $Z_\pm = n_\pm/n$ is comparable to 10 as long as the jet magnetization parameter is below 0.1 (Beloborodov 2010; Vurm et al. 2011). Far downstream of the shock, where the baryons have cooled, the inelastic collisions and the cascade end; here the pairs annihilate, if they still have time to do so before freezing out. The freeze-out happens when the outflow expansion timescale becomes shorter than the annihilation timescale; this occurs when the flow approaches the photosphere (Beloborodov 2010).

Note that neutrons can convert to protons (and protons to neutrons) in inelastic nuclear collisions. This enables the “converter” mechanism for baryon acceleration proposed by Derishev et al. (2003). Numerical results of Kashiyama et al. (2013) suggest that the converter mechanism becomes efficient for ultra-relativistic shocks, $\gamma_0 \gtrsim 4$.

9. DISCUSSION

This paper focused on sub-photospheric internal shocks in relativistic explosions, their dissipation mechanism and structure. One question of observational interest is whether the shocks are capable of producing ultra-relativistic electrons. Energetic electrons at large optical depths emit synchrotron radiation (without self-absorption) and thus boost the photon number carried by the flow, which is later released at the photosphere. Another interesting question is how the shock evolves and radiates as it approaches the photosphere.

As long as the flow is opaque and radiation dominates its energy density, photon transport plays a leading role in shaping the shock front. Its thickness is then comparable to the photon mean free path. The radiation-mediated shock (RMS) is not capable of electron acceleration by the standard Fermi mechanism, since the electron radiates its energy faster than it can cross the shock. Photons experience significant energy gains by crossing the shock back and forth multiple times. This “bulk Comptonization” upscatters photons up to the MeV band (in the fluid frame); further upscattering is hindered by the energy loss due to electron recoil in scattering. The photon upscattering beyond ~ 1 MeV is also stopped by the absorption reaction $\gamma + \gamma \rightarrow e^- + e^+$. The produced mildly relativistic e^\pm pairs immediately cool down due to fast Coulomb and IC losses.

All this would suggest that sub-photospheric shocks are inefficient in producing particles with energies $E \gg m_e c^2$ in the fluid frame. However, a more realistic shock picture significantly differs from the simple RMS, in particular when one takes into account that the outflow carries magnetic fields and free neutrons (see Figure 11). The shock wave is capable of generating ultra-relativistic electrons in two ways:

(1) A strong collisionless subshock forms in the RMS. We have shown that this is inevitable (even deep below the photosphere) if the flow is sufficiently magnetized. A

mildly relativistic collisionless subshock heats the electrons to an ultra-relativistic temperature T_e . Their IC emission breeds e^\pm pairs in the upstream and regulates the shock structure to a self-consistent state with the postshock temperature $kT_e \sim 10m_e c^2$ (Section 6.2). This temperature is high enough to generate interesting synchrotron radiation without self-absorption, which is strong for electrons with Lorentz factors $\gamma_e \lesssim 10$ (Vurm et al. 2011). The subshock fails to generate particles with $\gamma_e > 10$ if it is weak (the flow is weakly magnetized) while pair loading remains strong, $Z_\pm \sim 10^2$, due to the conversion of bulk-Comptonized MeV photons (Section 5.2). (2) Inelastic nuclear collisions inject e^\pm pairs with Lorentz factors $\sim m_\pi/m_e \sim 300$ in the fluid frame. This mechanism becomes particularly efficient if the outflow carries free neutrons, as they can migrate across the RMS, making the shock wave partially mediated by neutrons (Figure 11).

The synchrotron losses of energetic electrons generated by either mechanism imply significant photon production. The synchrotron photons may carry a small fraction of radiation energy, however, their *number* is significant. GRB jets tend to experience photon-starvation in the “Wien zone” at optical depths $10^2 < \tau_T < 10^5$ (Beloborodov 2013). In this zone, the heated photons have a Wien (rather than Planck) spectrum, i.e. a Bose-Einstein distribution with a non-zero chemical potential. The production of low-energy photons is followed by their quick Comptonization to the Wien peak. The addition of photons shifts the peak to lower energies, as the energy per photon is reduced. This effect regulates the observed peak position of the GRB spectrum that is eventually released at the photosphere (Vurm & Beloborodov 2016). Synchrotron photons produced outside the Wien zone, i.e. at smaller optical depths $\tau_T < 10^2$, are only partially Comptonized toward the Wien peak and form the low-energy part of the prompt GRB spectrum with the characteristic photon index $\alpha \sim 1$ (see Vurm & Beloborodov 2016; Thompson & Gill 2014).

Nuclear collisions in the shock front also generate neutrinos. Neutrino emission from migrating and colliding neutrons in GRB jets was previously discussed in some detail (Derishev et al. 1999; Bahcall & Mészáros 2000; Mészáros & Rees 2000a). The typical energy of neutrinos produced by this mechanism is $\sim \Gamma m_\pi c^2 \gtrsim 10$ GeV and they are detectable by IceCube (Bartos et al. 2013; Murase et al. 2013). Sub-photospheric internal shocks were also proposed to emit ultra-high-energy neutrinos (Mészáros & Waxman 2001; Razzaque et al. 2003). This proposal assumed efficient ion acceleration by the Fermi diffusive mechanism. This mechanism does not operate in an RMS. Diffusive acceleration is also suppressed in the collisionless subshock with a transverse magnetic field, which advects the particles downstream before they have a chance to cross the shock many times (Sironi & Spitkovsky 2011). An oblique magnetic field could help this process to occur.

Detailed studies of sub-photospheric shock structure require numerical simulations. Previous work focused on the search of a steady-state solution for the RMS (e.g. Levinson & Bromberg 2008; Budnik et al. 2010; Tolstov et al. 2015), which may be found by iterations. Instead, we suggest two techniques that permit

direct time-dependent simulations of shock formation, as demonstrated in Sections 4 and 5. Our simulations are set up to follow the evolution of an internal compressive wave, which leads to formation of a pair of shocks and their subsequent quasi-steady propagation. The shock structure is obtained from first principles, by simulating the time-dependent radiative transfer in the moving plasma.

We have implemented two methods for such simulations: (1) solving the radiative transfer equation coupled to the flow dynamics and (2) tracing individual photons and their interaction with the moving plasma using Monte-Carlo technique. Both methods show the structure of the established shock wave (Figures 8 and 9) and reproduce the jump conditions described in Section 3. The simulations verified the formation of a strong subshock in magnetized RMS. In particular, in GRB jets, a moderate magnetization ~ 0.1 is sufficient to generate a strong subshock.

A curious feature indicated in Figure 11 and discussed in Section 6 is the delayed cooling of the ions heated in the collisionless subshock. If the subshock is relativistic, the ion cooling length l_{Coul} can exceed the RMS thickness. When the ion energy is finally radiated, the produced radiation is trapped and advected downstream, missing the chance to diffuse upstream and affect the shock velocity profile. The delayed ion cooling also implies that some ions experience inelastic nuclear collisions and emit neutrinos even in the absence of a free neutron component.

We have estimated the pair-loading factor $Z_\pm \sim 10^2$ in the RMS with or without a collisionless subshock. The e^\pm pairs are produced in collisions between MeV photons, which are generated by two mechanisms. RMS without a strong collisionless subshock produces MeV photons only through bulk Comptonization in a relatively cold converging flow, which is close to Compton equilibrium with local radiation at $kT \ll m_e c^2$. In the presence of a collisionless jump, MeV photons are produced by IC cooling of e^\pm heated in the jump to $kT_e \sim 10m_e c^2$.

As the GRB jet expands from the central engine the structure of internal shocks and dissipation mechanism change. As long as the jet energy is dominated by radiation, $U_{\text{rad}} \gg \tilde{\rho} c^2$ and $U_{\text{rad}} \gg U_B$, the shock structure is described by a unique solution, which has no collisionless subshock (Figure 8). Bulk Comptonization in such deep sub-photospheric shocks is also suppressed, and their structure is conveniently described by the “force-free” radiative transfer solution for the bolometric intensity. This regime can occur at small radii in GRB jets, where the outflow Lorentz factor $\Gamma \ll \Gamma_{\text{sat}}$.

Nuclear dissipation due to neutron migration across the RMS increases with Γ and approaches its maximum near the radius of Lorentz factor saturation. It remains high until the neutron decoupling radius R_n , and then it declines as $(r/R_n)^{-1}$.

The shock “breakout” at the photosphere occurs through the growth of the collisionless subshock in the RMS until radiation completely decouples from the plasma. Eventually the entire velocity jump becomes mediated by collective plasma processes, regardless of magnetization. This somewhat resembles the shock breakout in non-relativistic supernova explosions (Waxman & Loeb 2001; Giacinti & Bell 2015). However, there is

a special feature: e^\pm pair creation near the collisionless shock sustains an optical depth $\tau_T \gtrsim 1$ even after the background electron-ion plasma becomes transparent. Effectively, the shock carries the photosphere with it until it expands by an additional factor ~ 30 , continually producing photospheric emission. This emission will be observed as a prominent pulse of nonthermal radiation in the GRB light curve.

In the observer frame, the emission from the e^\pm -dressed shock extends up to the GeV band, where γ - γ absorption shapes a break in the spectrum. The high-energy photospheric pulses overlap, in observer time, with the GeV flash that is produced by the e^\pm -loaded external blast wave at a larger radius $R \sim 10^{16}$ cm (Beloborodov et al. 2014; Hascoët et al. 2015). These pulses may explain the observed variable component of GeV emission superimposed on the smooth GeV flash at early times (Ackermann et al. 2013).

Internal shocks are a particularly promising heating

mechanism for jets that are not magnetically dominated. Comparison of detailed models of photospheric radiation with observed GRB spectra suggests a moderate magnetization in the sub-photospheric region, $\sigma \sim 10^{-2} - 10^{-1}$ (Vurm & Beloborodov 2016). This does not however exclude a stronger magnetization close to the central engine, allowing for magnetic dissipation that reduces σ as the jet expands. In this scenario, the early heating would be dominated by magnetic dissipation. Even in this regime shocks can occur and dissipate significant energy, as follows from the jump conditions discussed in Section 3.

I thank Hirotaka Ito, Christoffer Lundman, and Indrek Vurm for discussions and comments on the manuscript. This work was supported by NSF grant AST-1412485, NASA grant NNX15AE26G, and a grant from the Simons Foundation (#446228, Andrei Beloborodov)

APPENDIX

A. LOCATION OF SHOCK FORMATION IN A SUPERSONIC COMPRESSIVE WAVE

A supersonic wave converging toward the caustic $x = 0$ forms a pair of shocks at the Lagrangian coordinates $\pm x_0^*$. The value of x_0^* can be estimated as follows.

Consider the streamlines that experience smooth compressive deceleration, due to the conversion of kinetic energy to enthalpy. For a streamline with a given Lagrangian coordinate x_0 the characteristic time $t_{\text{dec}}(x_0)$ and location $x_{\text{dec}}(x_0)$ where deceleration occurs is given by Equations (9) and (10). Next, note that the smooth compressive deceleration to a subsonic speed is possible as long as the density of the gas accumulated in the subsonic region, ρ_{dec} , is comparable to the density of the ballistic flow approaching it,

$$\rho_{\text{bal}} \approx \frac{\rho_0}{1 + v'_0 t_{\text{dec}}}.$$

Since $\rho \propto P^{1/\alpha}$ and pressure in the subsonic region is not far from uniform (it tends to equilibrate on the sound crossing time), ρ_{dec} is roughly uniform,

$$\rho_{\text{dec}} \approx \frac{x_0}{x_{\text{dec}}} \rho_0. \quad (\text{A1})$$

The density ratio is given by

$$f(x_0) \equiv \frac{\rho_{\text{bal}}}{\rho_{\text{dec}}} \approx \frac{1 + v_0 t_{\text{dec}}/x_0}{1 + v'_0 t_{\text{dec}}}. \quad (\text{A2})$$

Using Equation (9), one can exclude t_{dec} and obtain

$$f(x_0) \approx 1 - \left(\frac{v_0}{v'_0 x_0} - 1 \right) \left[\left(\frac{(\alpha - 1)v_0^2}{2c_0^2} \right)^{1/(\alpha-1)} - 1 \right]. \quad (\text{A3})$$

The unity in the last term (in square brackets) may be neglected for streamlines with $v_0^2 \gg c_0^2$. One can see that $f < 1$ and f is close to unity for small $|x_0|$. It sharply drops when $|x_0|$ exceeds a characteristic x_0^* , and formally even changes sign. The characteristic x_0^* may be estimated from the condition $f \sim 0$.

For waves with amplitudes $v_{\text{max}} \gg c_0$ one finds that x_0^* is much smaller than the wavelength. Therefore, in the calculation of x_0^* one can use the Taylor expansion of the velocity profile around $x_0 = 0$,

$$v_0(x_0) = -a x_0 + \frac{b}{6} x_0^3 + \mathcal{O}(x_0^4), \quad (\text{A4})$$

where $a = -v'_0(0)$ and $b = v'''_0(0)$. Here we took into account that the second derivative v''_0 vanishes at $x_0 = 0$ (recall that we chose the zero x -coordinate at the location of the caustic where $-v'_0$ is maximum, see Section 2.1). A linear expansion $v_0 = -a x_0 + \mathcal{O}(x_0^3)$ would not be sufficient — a uniform $v'_0(x_0)$ would imply a uniform compression of the ballistic flow, with no pressure gradient that could cause deceleration. One can also see from Equation (A3) that it is the deviation from the linear velocity profile $v_0/v'_0 x_0 - 1 \approx b x_0^2/3a$ that controls the drop of f below unity, and hence controls shock formation.

For the supersonic streamlines with $v_0^2 \gg c_0^2$ Equation (A3) yields the relation

$$1 - f \approx \frac{b}{3a} x_0^2 \left[\frac{(\alpha - 1)a^2 x_0^2}{2c_0^2} \right]^{1/(\alpha-1)}, \quad (\text{A5})$$

and hence

$$x_0^{*2\alpha} \approx \frac{3^{\alpha-1}}{\alpha-1} 2c_0^2 a^{\alpha-3} b^{1-\alpha}. \quad (\text{A6})$$

The coefficients a and b in the Taylor expansion (A4) can be estimated as $a \approx p_{\max}c/L$ and $b \approx p_{\max}c/L^3$ for a smooth initial profile of the wave; these relations are exact for a sine profile $p_0(x_0) = -p_{\max} \sin(x_0/L)$. Substitution to Equation (A6) gives

$$\frac{x_0^*}{L} \approx \chi \left(\frac{c_0}{cp_{\max}} \right)^{1/\alpha}, \quad (\text{A7})$$

where $\chi \approx 3^{(\alpha-1)/2\alpha} [2/(\alpha-1)]^{1/2\alpha} \sim 2$ for the relevant range of $4/3 < \alpha < 2$. Numerical simulations (similar to the sample model shown in Figure 3, with different α and c_0) provide the accurate location of shock formation and confirm the scaling predicted by Equation (A7), with a slightly larger numerical coefficient $\chi \approx 3-4$.

REFERENCES

- Ackermann, M., Ajello, M., Asano, K., et al. 2013, *ApJS*, 209, 11
 Amato, E., & Arons, J. 2006, *ApJ*, 653, 325
 Bahcall, J. N., & Mészáros, P. 2000, *PhRvL*, 85, 1362
 Bartos, I., Beloborodov, A., Hurley, K., & Marka, S. 2013, *Phys. Rev. Lett.* 110, 241101
 Beloborodov, A. M. 1999, *MNRAS*, 305, 181
 Beloborodov, A. M. 2002, *ApJ*, 565, 808
 Beloborodov, A. M. 2003, *ApJ*, 588, 931
 Beloborodov, A. M. 2010, *MNRAS*, 407, 1033
 Beloborodov, A. M. 2011, *ApJ*, 737, 68
 Beloborodov, A. M. 2013, *ApJ*, 764, 157
 Beloborodov, A. M., Hascoët, R., & Vurm, I. 2014, *ApJ*, 788, 36
 Beloborodov, A. M., & Uhm, Z. L. 2006, *ApJL*, 651, L1
 Bromberg, O., Mikolitzky, Z., & Levinson, A. 2011, *ApJ*, 733, 85
 Budnik, R., Katz, B., Sagiv, A., & Waxman, E. 2010, *ApJ*, 725, 63
 de Hoffmann, F., & Teller, E. 1950, *PhRv*, 80, 692
 Derishev, E. V., Aharonian, F. A., & Kocharovsky, V. V. 2003, *PhRvD*, 68, 043003
 Derishev, E. V., Kocharovsky, V. V., & Kocharovsky, V. V. 1999, *ApJ*, 521, 640
 Daigne, F., & Mochkovitch, R. 1998, *MNRAS*, 296, 275
 Giacinti, G., & Bell, A. R. 2015, *MNRAS*, 449, 3693
 Hascoët, R., Vurm, I., & Beloborodov, A. M. 2015, *ApJ*, 813, 63
 Hoshino, M., Arons, J., Gallant, Y. A., & Langdon, A. B. 1992, *ApJ*, 390, 454
 Ginzburg, V. L., & Syrovatskii, S. I. 1964, *The Origin of Cosmic Rays* (Oxford: Pergamon)
 Ito, H., et al. 2015, 814, L29
 Kashiyaama, K., Murase, K., & P. Mészáros 2013, *Phys. Rev. Lett.*, 111, 131103
 Kobayashi, S., Piran, T., & Sari, R. 1997, *ApJ*, 490, 92
 Landau, L. D., & Lifshitz, E. M. 1959, *Fluid Mechanics* (Oxford: Pergamon Press)
 Lazzati, D., Morsony, B. J., Margutti, R., & Begelman, M. C. 2013, *ApJ*, 765, 103
 Levinson, A., & Bromberg, O. 2008, *Phys. Rev. Lett.*, 100, 131101 (LB08)
 Levinson, A. 2012, *ApJ*, 756, 174
 Medvedev, M. V., & Loeb, A. 1999, *ApJ*, 526, 697
 Mészáros, P., & Rees, M. J. 2000a, *ApJ*, 541, L5
 Mészáros, P., & Rees, M. J. 2000b, *ApJ*, 530, 292
 Mészáros, P., & Waxman, E. 2001, *Phys. Rev. Lett.*, 87, 171102
 Murase, K., & Ioka, K. 2013, *PhRvL*, 111, 121102
 Murase, K., & Kashiyama, K., & Mészáros, P. 2013, *PhRvL*, 111, 131102
 Ohsuga, K., & Takahashi, H. 2016, *ApJ*, 818, 162
 Pe’er, A., Mészáros, P., & Rees, M. J. 2006, *ApJ*, 642, 995
 Pe’er, A., & Waxman, E. 2004, *ApJ*, 613, 448
 Razzaque, S., Mészáros, P., & Waxman, E. 2003, *PhRvD*, 68, 083001
 Rees, M. J., & Mészáros, P. 1994, *ApJ*, 430, L93
 Ryde, F., et al. 2011, *MNRAS*, 415, 3693
 Sapir, N., Katz, B., & Waxman, E. 2013, *ApJ*, 774, 79
 Sironi, L., & Spitkovsky, A. 2011, *ApJ*, 726, 75
 Stern, B. E. 2003, *MNRAS*, 345, 590
 Stockem, A., Fiúza, F., Fonseca, R. A., & Silva, L. O. 2012, *ApJ*, 755, 68
 Svensson, R. 1984, *MNRAS*, 209, 175
 Svensson, R. 1987, *MNRAS*, 227, 403
 Thompson, C., & Gill, R. 2014, *ApJ*, 791, 46
 Thompson, C., & Madau, P. 2000, *ApJ*, 538, 105
 Tolstov, A. G., Blinnikov, S. I., & Nadyozhin, D. K. 2013, *MNRAS*, 429, 3181
 Tolstov, A., Blinnikov, S., Nagataki, S., & Nomoto, K. 2015, *ApJ*, 811, 47
 Vurm, I., & Beloborodov, A. M. 2016, *ApJ*, 831, 175
 Vurm, I., Beloborodov, A. M., & Poutanen, J. 2011, *ApJ*, 738, 77
 Waxman, E., & Loeb, A. 2001, *Phys. Rev. Lett.*, 87, 071101
 Weaver, T. A. 1976, *ApJS*, 32, 233
 Yu, H.-F., van Eerten, H. J., Greiner, J., et al. 2015, *A&A*, 583, A129
 Zeldovich, Y. B., & Raizer, Y. P. 1966, *Physics of Shock Waves and Hightemperature Hydrodynamic Phenomena* (New York: Academic)